



Master's Thesis in Experimental Physics

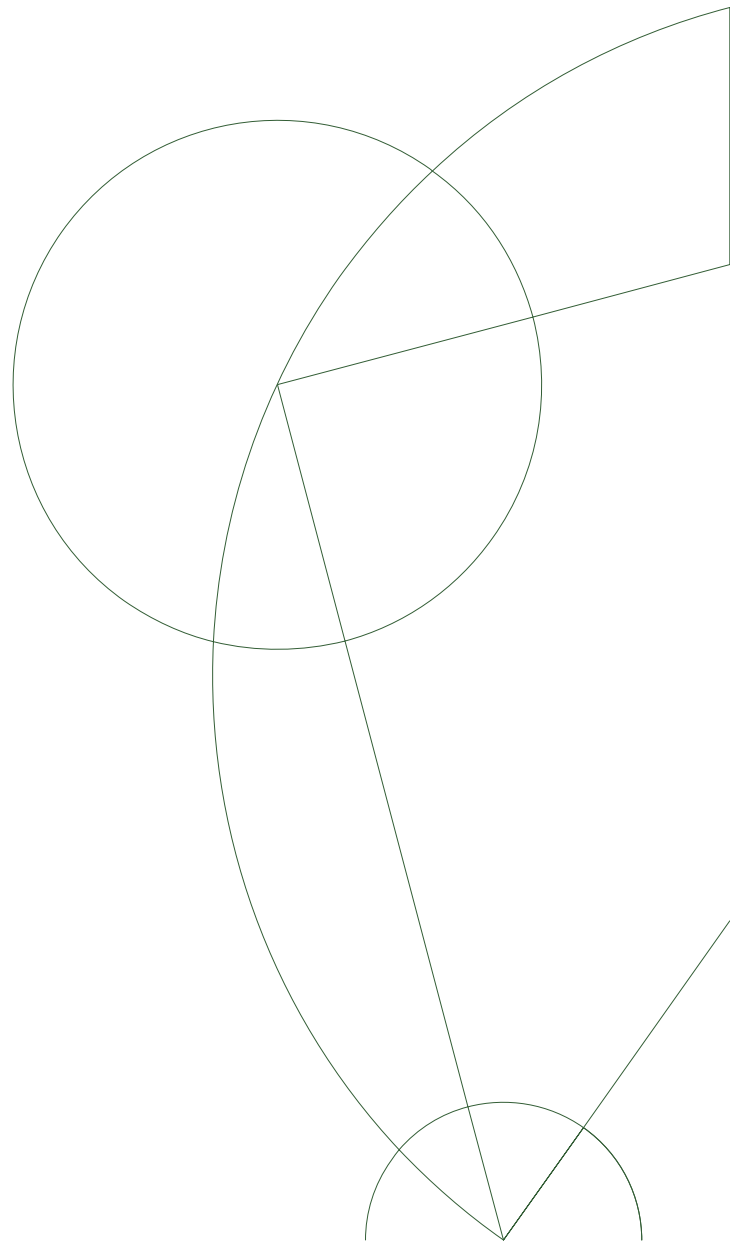
Morten Madsen
ctg850@alumni.ku.dk

Investigating timescales for quasi-particle poisoning
in superconducting quantum dots in InAs nanowires

Center for Quantum Devices

Supervisor: Charles M. Marcus

July 19, 2016



Acknowledgement

The last 15 months of working at the Center for Quantum Devices has been a rollercoaster. Starting up the next-generation of nanowire-based Majorana experiments has not been an easy task, but I could not have asked for better coworkers. Of these coworkers there is one guy who stands out from the crowd - Deividas Sabonis. A workhorse like no other, yet still chatty and always up for a short coffee break. Working with you is an inspiration. Thank you for always answering my (very often incredibly stupid) questions and for not yet having glued my mouth shut during one of my rants.

I would also like to thank Dovydas Razmadze who I would regard as a fabrication God. The devices you have fabricated since christmas are beautiful.

Other (current and previous) important people at QDev whose company I have been grateful to share is Sven Albrecht, Andrew Higginbotham, Fabrizio Nichelle, Ferdinand Kuemmeth, Hung Nguyen to mention those I have interacted with the most.

Furthermore I would like to thank Charles M. Marcus for giving me the opportunity to take (co-) charge of a brand new research programme in the world of Majorana zero modes.

Abstract

Long quasi-particle poisoning times is one of the most important features of a system for it to be used as a building block for topologically protected quantum information processing. In this thesis quasi-particle poisoning in semiconductor-superconductor nanostructures is investigated. The device used in the experiment consists of an InAs nanowire with an epitaxially grown 2-facet Al shell lithographically patterned into two superconducting islands. Read-out is performed using standard dissipative reflectometry technique using a second proximal nanowire functioning as the charge sensor.

This thesis reports timescales of quasi-particle poisoning events of up to 300 μs . This is, to my knowledge, the first experiment investigating the timescales of quasi-particle poisoning in a system shown to support Majorana zero modes [1]. Both measurement techniques and step-by-step procedures towards poisoning time extraction are reported. Furthermore suggestions on how the poisoning times can be improved in the next generation of devices are also given.

The timescales reported also suggests that nanowire-based Majorana zero mode systems have quantum state decoherence times similar to other solid state based approaches to quantum computing such as superconducting-qubits and spin-qubits. This indicates that it could act as a platform for planned future experiments involving demonstration of the non-abelian character of Majorana zero modes[2], an experiment whose device is lithographically similar to the one presented in this thesis.

List of abbreviations

- SC - Superconductor
- QP - Quasi-Particle
- QPP - Quasi-Particle Poisoning
- MZM - Majorana Zero Mode
- MF - Majorana Fermion
- UHFLI - Ultra High-Frequency Lock-In
- RF - Radio-Frequency
- DC - Direct Current
- AC - Alternating current
- BW - Bandwidth
- NW - Nanowire
- SEM - Scanning Electron Micrograph
- CB - Coulomb Blockade
- QD - Quantum Dot
- SQD - Superconducting Quantum Dot
- TQC - Topological Quantum Computing
- MBS - Majorana Bound State
- GND - ground
- SIN - Superconductor-Insulator-Normal metal
- ADC - Analog-to-digital converter

- DAC - Digital-to-analog converter
- VISA - Virtual Instrument Software Architecture
- GPIB - General Purpose Interface Bus
- SDK - Software Development Kit
- ASCII - American Standard Code for Information Interchange
- AWG - Arbitrary Waveform Generator
- MC - Mixing Chamber
- DMM - Digital Multi-Meter
- BNC - Bayonet Neill–Concelman
- SMA - SubMiniature version A
- TC - Tank Circuit
- VNA - Vector Network Analyzer
- QPC - Quantum Point Contact
- SNR - Signal-to-Noise ratio
- CPH board - Copenhagen board
- QDev - Center for Quantum Devices

Contents

List of figures	vii
1 Motivation	1
1.1 Majorana fermions in condensed matter	1
1.2 What is a Majorana particle?	2
1.3 Superconductors	3
1.4 Quantum dots	5
2 Experimental setup	8
2.1 Configuring the cryostat	8
2.2 Configuring the sample puck	11
2.3 Radio-frequency read-out	15
2.3.1 Impedance	15
2.3.2 Demodulation circuit	17
2.4 Electronics	17
2.4.1 ATS9360 - Alazar fast digitizer board	18
2.4.2 Zürich Instruments Ultra High-Frequency Lock-In	20
2.4.3 Sample clock synchronization	21
3 Measurements	22
3.1 Characterization of the device	22
3.2 Characterization of reflectometry	26
3.3 Quasi-particle poisoning events	29
4 Conclusion	40
A Pinout of Copenhagen sample board	41
B Fridge wiring	43
References	44

List of Figures

1.1	Density of states for a superconductor.	4
1.2	Normal and superconducting quantum dot energy parabolas	6
2.1	Sketch of SIN device as well as figures showing I vs. V_{SD} , extracted electron temperature, and the temperature fits to the data.	10
2.2	Photo and electrical schematic of RC and RF filters	11
2.3	Photo of daughterboard and electrical schematic of tank circuits. . .	13
2.4	Tank circuit resonance matching as a function of applied varactor bias.	14
2.5	LRC circuit schematic.	15
2.6	Demodulation circuit	18
2.7	AlazarCard acquisition 3-dimensionsal datacube	19
3.1	False-coloured SEM of device Q418DR3DDDEV1 used for the measurements	23
3.2	Supercurrent measurement	25
3.3	Tank circuit resonances as a function of applied gate voltage and extraction of matching resistance.	27
3.4	Configuration of cross-compensation for charge-sensing as well as raw and processed data of reflectometry signal.	28
3.5	Single dot device tuning.	30
3.6	Comparing expected pulse with pulse uploaded to AWG.	31
3.7	Energy diagram for superconducting quantum dot. Dummy, initialization and measurement segments of the pulse sketched.	32
3.8	Dependence on coupling to lower lead for qpp times.	33
3.9	Comparison of two situations coupling limited by either Γ_L or Γ_M . .	34
3.10	Initialisation time dependence for observed parity-dependent qp effects	35
3.11	Temperature dependence of quasi-particle poisoning time (16 - 230 mK).	36
3.12	Temperature dependence of quasi-partucle poisoning time (250 - 800 mK), including qpp time vs. MC temp.	37
3.13	Checking if dumme pulse introduces unwanted effects.	38

3.14	Checking half initialisation duration as well as inverting the pulse signal.	39
B.1	Fridge wiring for T10	43

1 Motivation

During the last year the field of quantum information science has seen tremendous progress. At the time of writing there are at least six different physical systems that could act as a potential platform for quantum computations. These include (1) superconducting quantum circuits (superconducting qubits) [3–7], (2) spin-qubits [8–11], (3) linear optical quantum computing [12, 13], (4) nitrogen vacancy centers (NVC) [14–16], (5) trapped ions [17–22], (6) nuclear magnetic resonance (NMR) [23–27], (7) ultra-cold atoms¹ [28], and even such exotic systems such as (8) biomolecular quantum computers [29].

Every system theoretically predicted to support quantum computations must satisfy certain rules first outlined by David DiVincenzo, and today widely regarded as *The DiVincenzo criteria* [30]. These criteria are:

1. A scalable physical system with well characterised qubits.
2. The ability to initialise the state of the qubits.
3. Long decoherence times.
4. A “universal” set of quantum gates.
5. A qubit-selective measurement capability.
6. The ability to interconvert between stationary and flying qubits.
7. The ability to transmit flying qubits between specified locations with high fidelity.

This thesis will primarily focus on the third of these criteria.

1.1 Majorana fermions in condensed matter

Ettore Majorana proposed the existence of Majorana Fermions (MF) as spin-1/2 particles described by a real field ϕ in 1937 [31]. This means the MF is its

¹Mostly acting as quantum simulators rather than general purpose quantum computers

own antiparticle, and was thought only to exist in particle physics. For example the neutrino is thought to act as a potential candidate for Majorana fermions.

In recent years, however, the condensed matter community has taken in the idea of Majorana Fermions as zero-energy excitations [32]. Majorana bound states in condensed matter systems are predicted to possess non-abelian particle statistics [33]. This means that if one has two particles described by $\psi_1(r_1)$ and $\psi_2(r_2)$ and a time-evolution of ψ_2 sends it from r_2 to r_1 and back to r_2 , then the phase acquired by the wavefunction depends on the path taken around ψ_1 . Recently several experimental groups have reported signatures of Majorana type excitations in condensed matter systems that provide strong evidence for the existence of Majorana Bound States [1, 34–36].

1.2 What is a Majorana particle?

A Majorana particle is predicted to be its own anti-particle which means it must be a zero-energy particle. In the language of second quantization it is said that

$$\gamma = \gamma^\dagger \tag{1}$$

where γ^\dagger (γ) is the creation (annihilation) operator for a Majorana fermion. Furthermore the number operator for Majorana particles $\gamma^\dagger\gamma$ has the property that

$$\gamma^\dagger\gamma = \gamma^2 = 1, \tag{2}$$

unlike for example in the case of fermions where it is either zero or one.

Furthermore a MBS must satisfy the commutator relation

$$[\hat{H}(\gamma_i), \gamma_j] = 0, \tag{3}$$

that is, the Majorana operator commutes with the Hamiltonian of the system (up to an exponentially small factor decreasing as the distance between γ_i and γ_j increases). This exponential protection of the Majorana bound state was recently shown experimentally [1].

1.3 Superconductors

Superconductivity was first discovered by H. K. Onnes in 1911 in Leiden [37], a discovery he was later awarded the Nobel Prize for. He noticed that after cooling down certain materials below a critical temperature T_C consistently show unmeasurably small resistances. Universal mechanisms responsible for SC is to this day still not known, and different superconducting materials have been shown to have different physical explanations for why they turn superconducting. Amongst the most well known classes of superconductors are pure elements (such as lead and aluminium), alloys such as niobium-titanium (NbTi), and cuprates such as yttrium-barrium-copper (YBCO).

Superconductors are known to be made out of a special type of quasi-particles known as cooper-pairs which, in the case of an s -wave superconductor, is a bound state of two electrons of opposite spin living at the Fermi energy. In the experiments reported in this thesis a thin-film superconductor made of Aluminium (Al) is used.

Density of states When a material transitions into the superconducting regime a gap is opened around the Fermi-energy ε_f known as the superconducting gap, and is denoted by 2Δ , see **fig.** 1.1. The region at $\varepsilon_f - \Delta$ is the ground-state of the system filled with Cooper-pairs and the region at $\varepsilon_f + \Delta$ is where quasi-particles live.

Josephson effect In 1962 B. D. Josephson predicted new effects for tunneling between two superconductors [38]. Even in the absence of an applied voltage difference between the two superconductors a *supercurrent* would flow

$$I_S = I_C \sin(\Delta\varphi), \quad (4)$$

with I_C the critical current of the junction and $\Delta\varphi = \varphi_1 - \varphi_2$ the phase difference between the two superconductors. This is known today as the DC Josephson effect or the Josephson current-phase relation.

Another important effect predicted by B. D. Josephson is that if a constant voltage across the junction is maintained the phase difference $\Delta\varphi$ between the two

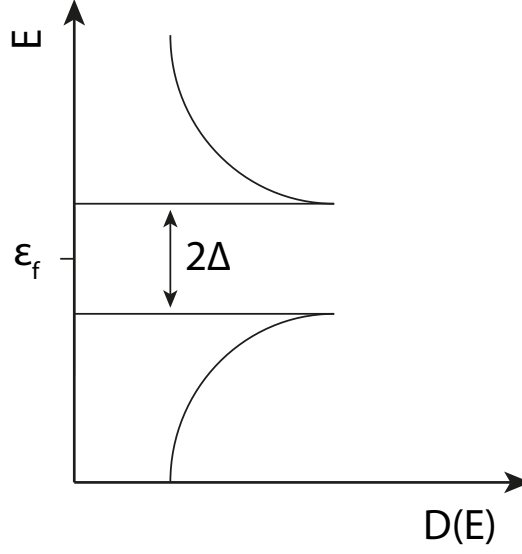


Figure 1.1: Density of states as a function energy $D(E)$. In the superconducting regime an energy gap of order 2Δ opens above and below the Fermi-energy ε_f .

superconductors would evolve in time as

$$\frac{d\Delta\varphi}{dt} = \frac{2e}{\hbar}V, \quad (5)$$

which is now known as the AC Josephson effect or the Josephson energy-phase relation.

An important energy scale in this experiment is the Josephson energy. We know that energy is given as

$$E = - \int dt UI. \quad (6)$$

Inserting (4) and (5) (first expressing it as a time-dependent potential $V(t)$) the energy between the two superconductors is

$$E = - \int dt \frac{\hbar}{2e} \frac{d\Delta\varphi}{dt} \cdot I_C \sin(\Delta\varphi) \quad (7)$$

$$= - \frac{\hbar}{2e} \int d\Delta\varphi \sin(\Delta\varphi) \quad (8)$$

$$= \frac{\hbar}{2e} \cos(\Delta\varphi). \quad (9)$$

As such the Josephson energy depends (up to an integration constant) on physical constants and the phase difference between the two superconductors.

1.4 Quantum dots

A quantum dot is simply put an isolated object capable of carrying charge. Typically the single-particle level-spacing is too small for it to be observed but in the presence of strong Coulomb interactions this is no longer the case. I would like to briefly mention the electrostatic energy of a quantum dot in both the normal and superconducting, although they are very similar. The superconducting case will be discussed in two limits $\Delta > E_C$ and $\Delta < E_C$.

Normal case When you have an isolated object capable of carrying charge then the number of electrons n is a good quantum number due to the Coulomb interactions which start to appear as more electrons are added to the dot. Even though the electrons, which the system is described by, are quantum mechanical phenomena the charging energy E_C of the quantum dot is a purely classical property.

When dealing with a normal quantum dot the electrostatic energy can be written as

$$E_{\text{el.}}^N(n_g) = E_C(N - n_g)^2, \quad (10)$$

where E_C is the charging energy given by $E_C = e^2/(2C_\Sigma)$, C_Σ the sum-total capacitance of the system, N is the number of electrons on island and n_g represents an effective number of electrons induced by a nearby gate electrode. This means that the electrostatic energy of a quantum dot is a series of shifted parabolas (see **fig. ??** and at the point where $E^N = E^{N+1}$ there's a degeneracy between the N and $N+1$ state and moving slightly to the right (the left) will favour adding (removing) an electron from the system, and transport through the island can be seen if we couple it to a source and a drain.

Superconducting case For the superconducting case the electrostatic energy of the quantum dot is almost the same except for an extra parity-dependent term $p_N E_0$ added yielding

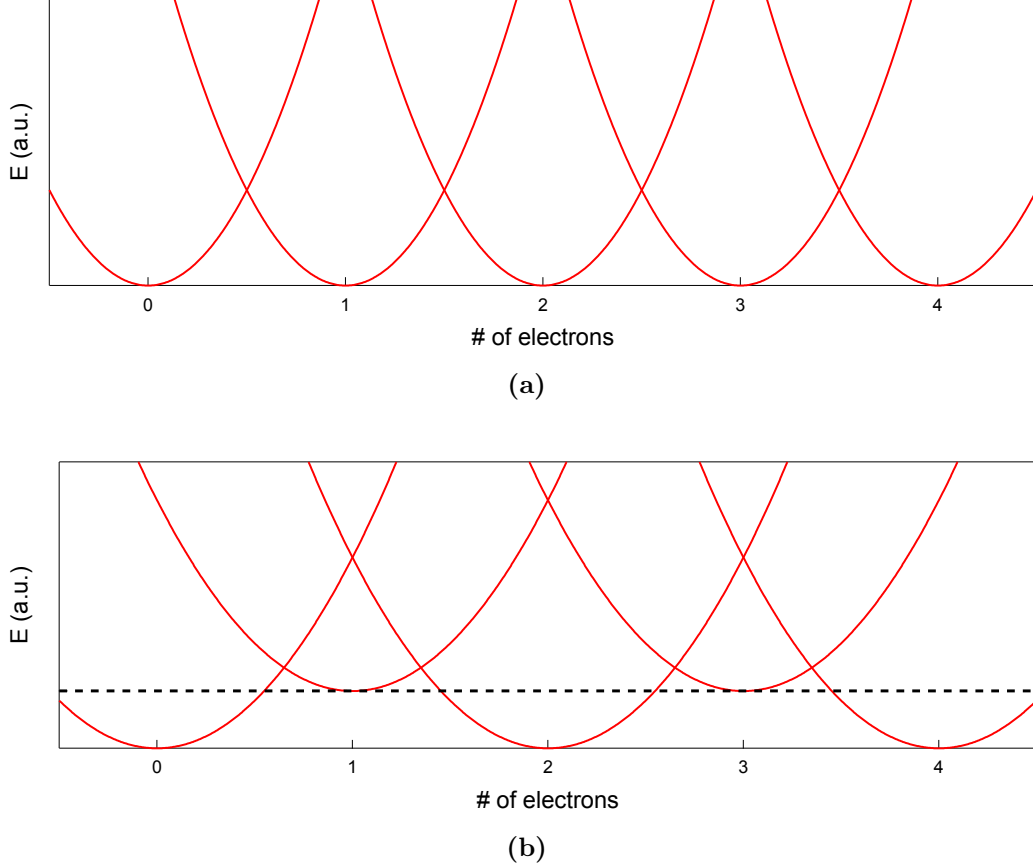


Figure 1.2: Sketch of the energy diagrams in the case of a normal (a) and superconducting (b) quantum dot. For the superconducting quantum dot the parabolas are drawn in the $\Delta < E_C$ regime.

$$E_{\text{el.}}^N(n_g) = E_C(N - n_g)^2 + p_N E_0 \quad (11)$$

where E_0 is the quasi-particle energy associated with adding a single electron to a superconducting island and p_N is the parity operator which is either 0 (even parity) or 1 (odd parity). The overall effect is that all odd parabolas are given an offset from zero energy in the parabola picture, and the offset is given by the quasi-particle energy E_0 which, in the case of a superconductor is the superconducting order parameter Δ .

If we are in the regime where this quasi-particle energy is larger than the charging energy of the island then it would be unfavourable to add an extra electron

in this excited state and as such only cooper-pairs are added to the quantum dot. Schematically this means that the odd parabolas will intersect with the even parabolas above the charge-degeneracy point of these. On the other hand if we are in the regime $\Delta < E_C$ then the odd parabola intersect the two even ones below this degeneracy point and single electrons are added to the island.

2 Experimental setup

The first section will be dedicated to some of the things one should be aware of when setting up a laboratory from scratch. After that I will touch upon the sample boards we use in our experiment, what it consists of and what its capabilities are. Then I will move on to talk about some of the most important electronics that we use in our experiment such as the ATS9360 fast digitizer board from AlazarTech and the Zürich Instruments Ultra High-Frequency Lock-In (UHFLI).

2.1 Configuring the cryostat

During fall 2015 the experimental facilities at QDev got expanded. Our clean-room was expanded, a new SEM from JEOL was installed, and, maybe most importantly, four new cryostats were installed on the 1st floor expanding the previous available cryostats from 7 to 11. On the 4th floor cryostats are of the type Triton 200 supplied by Oxford Instruments and only support use of, what we refer to as, small pucks. The 1st floor on the other hand is equipped with Triton 400 cryostats, also supplied by Oxford Instruments, and support use of large pucks. There are a couple of important differences between the two cryostats, one being the amount of cooling power they provide. Triton 400 cryostats provide 400 μW of cooling power at 100 mK whereas Triton 200 cryostats provide 200 μW . Another difference is, as mentioned, the type of sample pucks they support which naturally extends into a difference in the number of DC and coax lines available for experimentalists using a specific cryostat.

In this section I will touch upon electron thermometry measurements we did before installing filtering in the new cryostats. Afterwards I will talk about the filtering installed and some of the issues we encountered.

Electron thermometry It is important to ensure good thermalization of the electrons hitting the sample in order to avoid temperature broadening of the features we are interested in seeing, which in our case would be Coulomb features and superconductivity features. To perform electron thermometry we need a system which enables us to measure a feature which amongst other things depends on the electron temperature, but with the remaining parameters independently estimatable

from other measurements. Two such ways of performing electron thermometry are via Coulomb blockade and via a tunnel-junction device geometry. For this experiment we used a superconductor-insulator-normal metal (SIN) device made from Al–Al₂O₃–Cu provided by the PICO-group at Aalto University School of Science, Finland. The device consists of two large contacts which have a small overlap thus creating our tunnel-junction. A sketch of the SIN device can be seen in fig. 2.1 as well [39] which also contains a false-coloured scanning electron micrograph of a similar device.

We measure the current across the junction as a function of applied bias voltage which below 1.2 K, the critical transition temperature of Al, will show a distinct suppression of current through the device when the applied bias is less than the superconducting gap of Al. Following the methodology outlined in [39] we use their eq. (4) which in the regime $k_B T_{N,S} \ll eV_{SD}, \Delta(T_S)$ states that the electron temperature can be estimated as

$$T_N = \frac{e}{k_B} \frac{dV}{d \ln(I)}, \quad (12)$$

i.e. by fundamental constants and the slope of the high-bias current as a function of bias voltage.

The electron thermometry show that that the actual electron temperature on the sample was in the 100 - 150 mK range even though the ruthenium oxide (RuO₂) thermometer on the mixing chamber plate shows 20 mK or less. As such the filtering was required and later also installed. The RC and RF filters are thermally anchored to the mixing chamber plate using gold plated copper brackets. Since the cryostats on the 1st floor has 96 DC lines, corresponding to four looms, then we need four RC and RF filters. A single bracket provides the full RC and RF filtering for one loom and as such a total of four brackets mounted to the mixing chamber plate is needed. Since the mixing chamber plate is one of the smallest (in terms of diameter) plates disregarding the coldfinger there are severe space constraints to be considered. As such two filters were stacked onto each other but this brings another issue into play; how do we ensure sufficient cooling of the lower filter bracket? The solution is to wrap the lower bracket in copper braid which is then put in thermal contact with the mixing chamber plate by inserting the braid

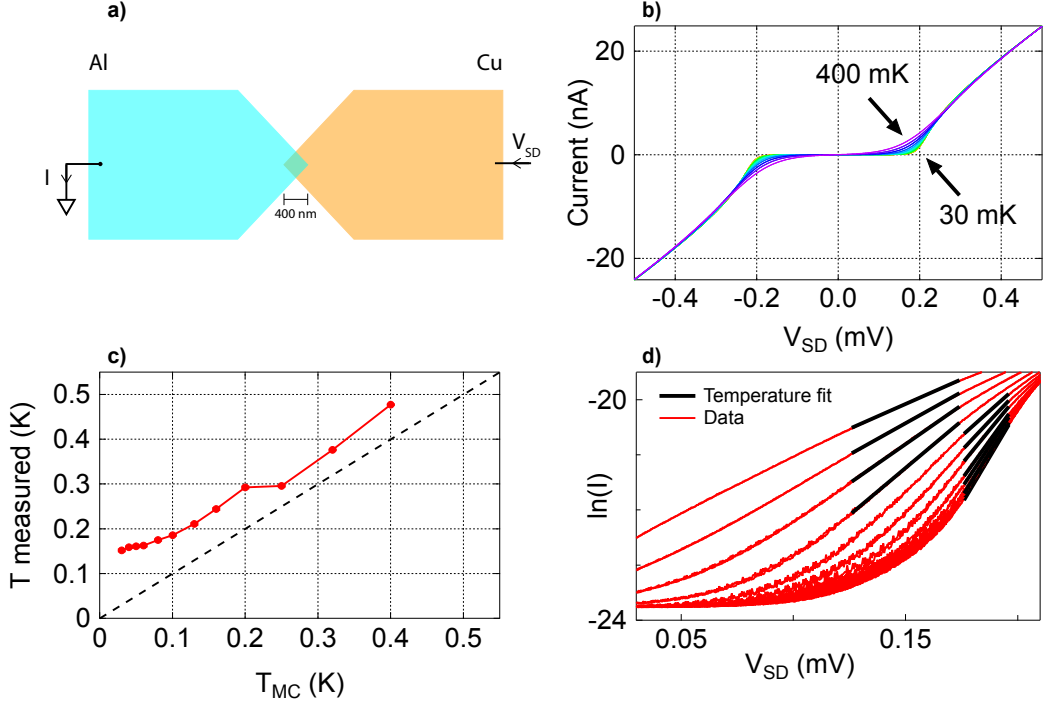


Figure 2.1: Summary of the data for the electron thermometry performed in Triton 10. Panel **a)** shows a sketch of the SIN device geometry *not* drawn to scale. Al (blue) and Cu (orange) indicated. Overlap between Al and Cu indicated. V_{SD} is the applied bias voltage, I the current across the tunnel-junction. Panel **b)** shows the current, I , across the junction as a function of applied bias voltage, V_{SD} measured at temperatures ranging from 30 mK to 400 mK. Panel **c)** shows the electron temperature extracted from the fits shown in panel **d)**. A black dashed diagonal line shown as a guide to the eye. It can be seen that the extracted electron temperature is always higher than the expected mixing chamber temperature, and is saturated at 150 mK. Error bars not shown as they are hidden within the point-marker. Panel **d)** shows a zoom-in of the data (red) in panel **b)** as well as the linear fits (black) made in the high-bias regime for extraction of the slopes.

between the plate and the bracket. A photo of the RC and RF filters is shown in **fig. 2.2**.

RC and RF filtering The first stage of the RC filter is a 7-pole π filter with a cut-off frequency of $f_c = 80$ MHz. The second and third stages are both an RC low-pass filter with $R_2 = 500 \Omega$ and $C_2 = 2200$ pF, and $R_3 = 1200 \Omega$ and $C_3 = 1000$ pF, respectively.

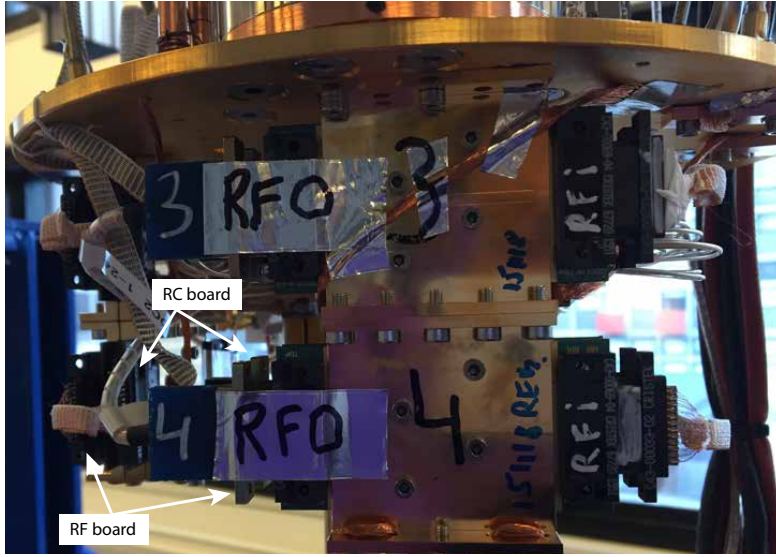


Figure 2.2: Photo of RC and RF filters used in the cryostats on the 1st floor.

In order to avoid stray magnetic fields inside the cryostat as many parts as possible are made from non-magnetic materials. Unlike the RC and RF filters used on the 4th floor the RC and RF filters for the 1st floor were attempted to be made using non-magnetic components. In thin film resistor manufacturing the most common resistive film used is Nichrome (NiCr) but the non-magnetic resistors (from Vishay Intertechnology, Inc. at least) are made using a Tantalum-Nitride (TaN_2) resistive film [40]. It was discovered during one of the early cooldowns that the resistors in the RC filters and on the Copenhagen sample boards went superconducting below 1.5 K. As such the filtering as well as the Copenhagen sample boards used in T8 through T11 was updated with non-superconducting resistors.

2.2 Configuring the sample puck

In QDev we have, at the time of writing, three different kinds of sample boards in use - Mayo boards, QDev boards and Copenhagen boards. For this experiment the Copenhagen board sample system is used since it gives access to 48 DC lines and up to 16 RF lines if the tank circuits are not in use, otherwise 15 RF lines and up to four tank circuits are available. All 16 RF lines are form a bias-tee with

a DC line via a (bias) resistor. A pinout sheet for the copenhagen board can be seen in appendix A which we use whenever a new sample is prepared for loading. Like the QDev board sample system the Copenhagen board sample system is also a modular sample system consisting of three parts: a motherboard, an interposer and a daughterboard.

Motherboard The motherboards serve as the main hub for all of the routing of the DC and RF signals as well as filtering of the DC signals and bias-tee's for the RF signals. Each motherboard supports up to 48 DC lines via two 51-pin nanoD connector and 16 RF signals via two 8-pin minicoax connectors². The reason for having two 51-pin nanoD connectors is to enable users to either do bias cooling (which is common practice in the 2DEG community [42]) or to ground the sample from the moment it is loaded into the puck until measurements at base temperature begins.

Currently we have two versions of the copenhagen motherboards which are manufactured using different dielectrics (and manufacturers). Some of the motherboards are made using FR-04, and others are made using Roger's RO3003 dielectric whose dielectric constant is much less frequency dependent. The two boards are easily distinct as FR-04 is coated in a green mask and the RO3003 is coated in a dark blue mask.

Daughterboard The daughterboard offers users independent DC lines (with RC filtering on the motherboard), bias-tee's as well as tank circuits. An image of front view of a daughterboard and an electrical schematic of the four tank circuits is shown in **fig. 2.3**. Here BX are the DC bias offset of the rf-carrier applied to the sample. VX were intended to be used as the voltage bias of the varactor(s), which were included in the tank circuit to be able to *in situ* tune the matching resistance of the resonance circuit [43], but during the first cooldown we noticed that our varactors freeze out below 1 K making it more or less impossible to tune the circuit into matching by changing the varactor bias, see **fig. 2.4**. As such we decided to completely remove the varactors from the daughterboards, enabling us to see the change in matching as we change the sensor wire resistance, see **fig. 3.3**.

²The minicoax connector is a proprietary connector from Rosenberger.

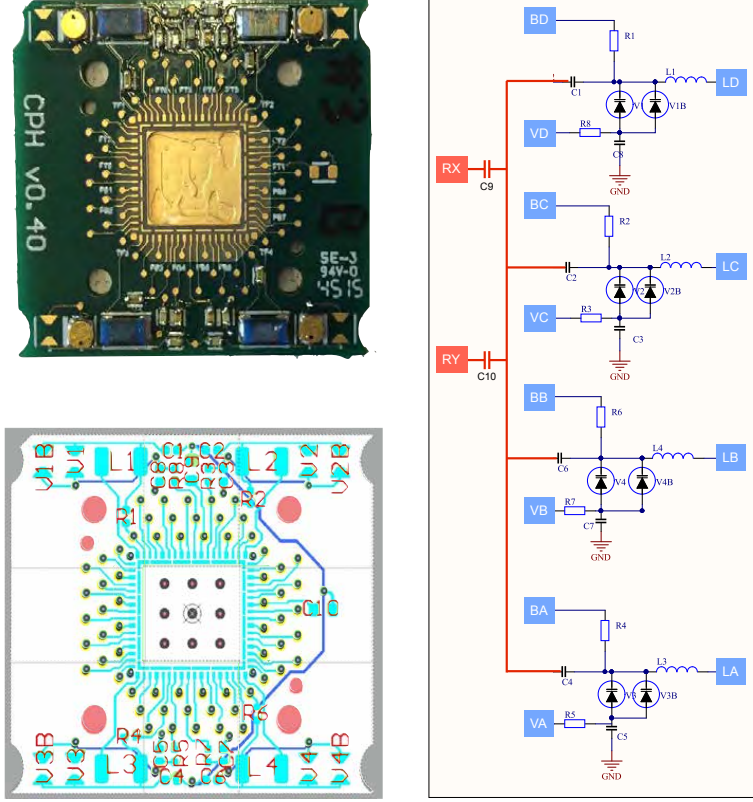


Figure 2.3: To the left is a photo of the daughterboards used for this experiment with all four tank circuits (incl. varactors) soldered.

Inductors Choosing the right inductors for your experiment is no trivial task. You need to make sure that the resonance frequency of the inductor is within the range of your electronics equipment such as (arbitrary) waveform and signal generators. Typically for experiments the parasitic capacitance for the tank circuit is of the order ~ 1 pF and as such the only variable in estimating the resonance frequency in (24) is the inductance. On the other hand, you also want to know the typical resistances the sensor device will be operated at as the matching resistance of the resonance circuit depends on the inductance. Our first choice of inductors were $L_1 = 390$ nH, $L_2 = 520$ nH, $L_3 = 860$ nH, and $L_4 = 1200$ nH. However we're only operating two tank circuits at any particular time and thus we only used L_2 and L_4 . Using (27) the matching resistances for these inductances are $R_2 = 11.2$ k Ω and $R_4 = 24$ k Ω , which correspond to $g_2 \sim 2.3 e^2/h$ and $g_4 \sim 1 e^2/h$.

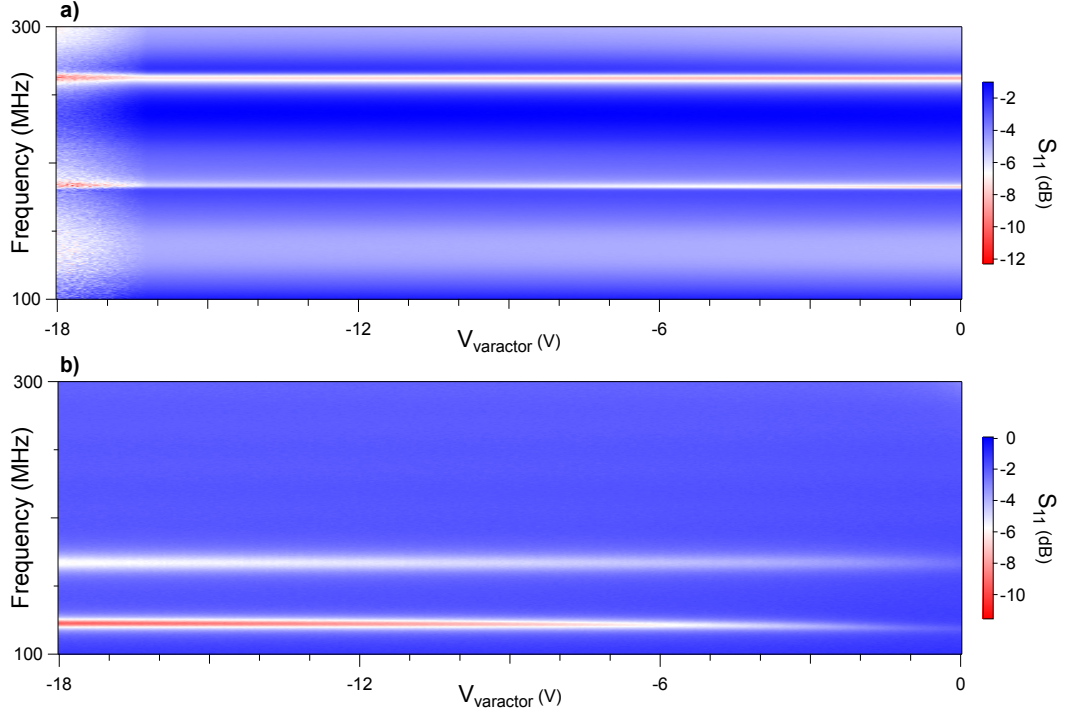


Figure 2.4: Tank circuit resonance matching as a function of applied varactor bias. Panel **a)** and **b)** shows how the tank circuits can be tuned into matching by applying a bias voltage to the varactors. **a** is taken at base temperature and **b** is taken at room temperature. Notice how at base temperature the resonance matching is unaffected by the applied varactor bias whereas at room temperature the resonances show a clear change as a function of varactor bias.

Our typical operating point for the sensor nanowires is somewhere between $0.1 e^2/h$ and $0.5 e^2/h$ which means that the inductances previously chosen are a little too low for the device to be close to matching while being operated as a sensor. Therefore we decided to switch the 820 nH inductor out with a 4.7 μH inductor which would give us an estimated matching resistance of about $g_{\text{est}} \sim 0.27 e^2/h$ which would be ideal for the experiment. However both times we've tried to cool down a daughterboard with the 4.7 μH inductor that section of the sensor wire has not been working so we do not know what the experimental matching resistance will be for this inductor.

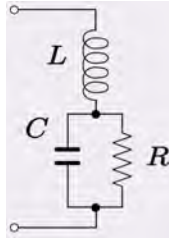


Figure 2.5: An LRC circuit schematic identical to the resonance circuit used in the experiment. Here L is the inductor on our sample board, C the parasitic capacitance of the bondwire and bondpad, and R is the resistance of the sensor wire.

2.3 Radio-frequency read-out

High-frequency techniques in recent years gained a lot of attention from the research community due to their high bandwidth while maintaining a high sensitivity. This allows the study of processes occurring on timescales inaccessible with standard lock-in techniques. While typical lock-in modulation frequencies are within audio frequency giving timescales of milliseconds, microwave techniques offer accessibility of timescales of the order of nanoseconds. What is more, acting at high frequencies help us to reduce $1/f$ -noise. Since microwave techniques enables nanosecond time-resolution physical processes such as qubit relaxation times as well as quasi-particle poisoning times can be investigated. The ultimate goal of single-shot read-out of quantum states is also only accessible using high-frequency techniques.

As a last thing it needs to be mentioned that high-frequency modulation techniques are much less prone to environmental disturbances and thus gives a much more robust way of carrying information about the quantum state under investigation.

2.3.1 Impedance

In circuit theory the three most well-known circuit elements are resistors, capacitors and inductors. Of these three elements the resistor is special since it is a dissipative, non-dispersive element whose resistance is frequency independent, whereas for capacitors and inductors this is not the case. When dealing with low-frequency (< 100 kHz) voltages a purely resistive approach is sufficient to account

for the behaviour of the circuit. However as frequency is increased and frequency-dependent components such as capacitors and inductors are added this is no longer the case and the circuit description needs to be modified. Since capacitors and inductors are reactive elements (i.e. non-dissipative) their "resistance" is imaginary and frequency dependent. This "resistance" is known as an impedance.

For resistors, capacitors and inductors the impedances can be shown to be

$$Z_R = R, \quad (13)$$

$$Z_C = 1/i\omega C, \quad (14)$$

$$Z_L = i\omega L, \quad (15)$$

respectively.

Resonance circuit and reflectometry Doing dissipative reflectometry you are detecting a change in resistance of the device. This changes the overall impedance of the resonance circuit which changes the reflected signal.

The resonance circuit used in this experiment is diagrammatically shown in **fig. 2.5**. We have an inductor on the sample board in series with a capacitor and a resistor, which are in parallel. The capacitance here is the parasitic capacitance of the wirebond from sample board to bondpad as well as the capacitance from the bondpad itself. The resistance is the resistance of the sensor wire.

The impedance of this resonance circuit is given by

$$Z_{LRC} = Z_L + \frac{1}{Z_C^{-1} + Z_R^{-1}} \quad (16)$$

$$= -i\omega L + \frac{R}{1 - i\omega CR} \quad (17)$$

$$= -i\omega L + \frac{R + i\omega CR^2}{1 + (\omega RC)^2}. \quad (18)$$

$$= \frac{R}{1 + (\omega RC)^2} + i\omega \left(-L + \frac{i\omega CR^2}{1 + (\omega RC)^2} \right) \quad (19)$$

Now to achieve maximal absorption of the rf-carrier signal in the tank circuit the impedance should be matched to the line impedance which is 50Ω . Therefore

we set $\text{Re}[Z_{LRC}] = 50$ and $\text{Im}[Z_{LRC}] = 0$. The latter yields

$$0 = \omega \left(-L + \frac{i\omega CR^2}{1 + (\omega RC)^2} \right) \Leftrightarrow \quad (20)$$

$$L = \frac{CR^2}{1 + (\omega RC)^2} \Leftrightarrow \quad (21)$$

$$(\omega RC)^2 = \frac{CR^2 - L}{L} \Leftrightarrow \quad (22)$$

$$\omega_0 = \sqrt{\frac{CR^2 - L}{LR^2C^2}} = \sqrt{\frac{1}{LC} - \frac{1}{R^2C}} \quad (23)$$

$$\approx \frac{1}{\sqrt{LC}}, \quad R, C \gg 1, \quad (24)$$

which is also known as the resonance frequency of the resonance circuit.

Using this result the first equation yields

$$50 = \frac{R}{1 + \frac{R^2C}{L}} \quad (25)$$

$$= \frac{LR}{1 + R^2C} \quad (26)$$

$$\approx \frac{L}{RC}, \quad R, C \gg 1, \quad (27)$$

which is the equation we use to estimate the matching resistance of our circuit.

2.3.2 Demodulation circuit

The demodulation used in our experiment is shown in **fig. 2.6**. Unlike typical demodulation circuits the circuit used here is primarily functioning via digital post-processing of the digitized signal from the Signal Input, see **sec. 2.4.2**

2.4 Electronics

This section is dedicated to explaining some of the most important electronics on which rely on heavily for our experiment. I want to mention a few things about our fast digitizer board followed by our new Ultra High-Frequency Lock-In from Zürich Instruments. Finally I'll briefly talk about synchronisation of electronics when you want to do fast read-out.

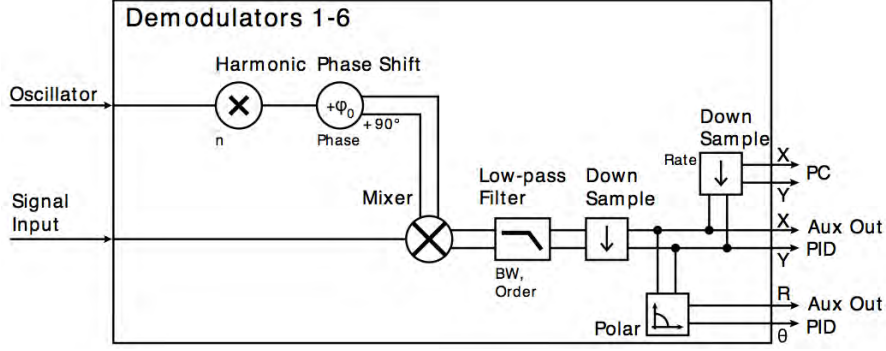


Figure 2.6: Diagram of the demodulation circuit used for this experiment. The signal is digitized by the Signal Input ADC and then sent through a mixer which is also supplied with the local oscillator signal. After mixing of the RF and LO signal the IF signal is sent through a low-pass filter and down-sampled from 1.8 GS/s to (maximally) 14 MS/s. Afterwards signal is sent via the auxiliary output to the signal input channel of our fast digitiser board in the data acquisition PC.

2.4.1 ATS9360 - Alazar fast digitizer board

For the 1st floor data acquisition PCs the Alazar ATS9360 fast digitiser board was purchased which differs from the fast digitiser board which is used on the 4th floor which is the ATS9440 model. The two cards are almost identical but differ in a few key areas, mainly the number of input channels, ADC bit resolution, max sampling speed, and input voltage range, see table 1. Given that our AlazarCard has a 12-bit ADC the voltage resolution of the input signal is $\sim 200 \mu\text{V}$, and the maximal time resolution we can record data at is $\sim 555 \text{ ps}$. However there are other constraints in the setup which sets an upper limit for the time resolution we require and so by the help of a lower sampling speed and internal averaging the typical time resolution of a data point is $\sim 100 \text{ ns}$.

Since the AlazarCard is integrated into the computer hardware (it sits in a PCIe 8x slot on the motherboard of the computer) typical ASCII commands sent via Virtual Instrument Software Architecture (VISA) or General Purpose Interface Bus (GPIB) cannot be used. A dynamic library is provided by the AlazarTech software development kit (SDK) meaning that in order to get it integrated into our IGOR data acquisition suite an IGOR XOP (IGOR External Operation) file has to be generated. The first XOP for the AlazarCards was compiled by James Medford for the spin-qubit experiments at Harvard and is currently the exact same

Model	# of channels	ADC res.	Max sampling speed	Input voltage range
ATS9440	4	16 bit	125 MS/s	$\pm 100 \text{ mV} - \pm 4 \text{ V}$
ATS9360	2	12 bit	1.8 GS/s	$\pm 400 \text{ mV}$

Table 1: A comparison of the ATS9440 and ATS9360 fast digitizer cards from AlazarTech. Information shown is the number of input signal channels available on the fast digitizer card, the number of bits available in the ADC (analog-to-digital converter), the maximum sampling speed the card can handle (the inverse being the time resolution of each point acquired), and the input voltage range of the input channels. Whereas the max sampling speed is a global setting on the AlazarCard (i.e. it applies to all channels) the input voltage range (as well as the input impedance) of the channels can be set locally.

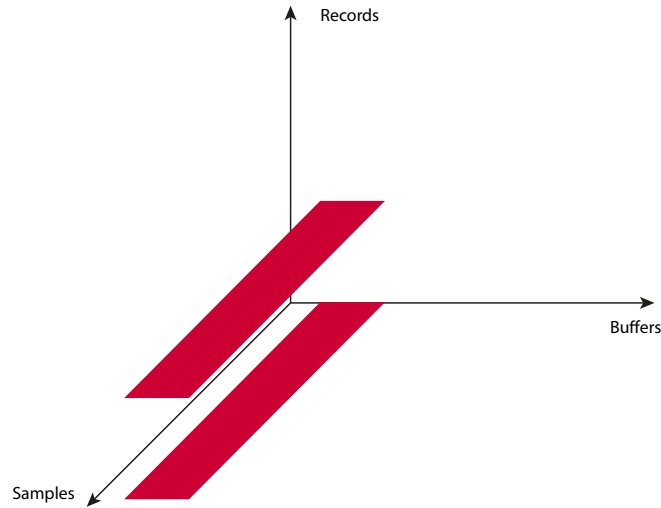


Figure 2.7: Rough sketch of the 3-dimensional datacube showing how the AlazarCard acquires data.

XOP we're using. However with the increased sampling speed of our AlazarCard we've run into a few issues which were not evident before. One issue associated with the XOP is that by specifying a certain amount of data to be acquired by the AlazarCard we're able to crash windows by trying to allocate data into memory which isn't available (it isn't there). Another issue, which is an IGOR 32-bit issue, is that at some point the waves we're trying to generate become too big for the 32-bit version to handle which then crashes IGOR.

The AlazarCard acquires data in a 3-dimensional cube, see **fig. ??**. This is

done by us sending a command to the AlazarCard requesting data. In that call we specify number of samples, records and buffers we want. For the measurements shown in [sec. 3.3](#) N samples was requested, 1000 records and a single buffer. In this case the records act as a way of taking 1000 identical shots of the same data, then compressing it (i.e. averaging it together) into a single line. Increasing the number of buffers is one way to acquire a 2D image using the AlazarCard in a matter of seconds.

2.4.2 Zürich Instruments Ultra High-Frequency Lock-In

The Zürich Instruments Ultra High-Frequency Lock-In (UHFLI) is intended to be a digital single-unit replacement of the signal generator, pre-fridge attenuation, post-sample circuit for demodulation of the reflected rf-signal, and also ultimately handle the fast digitization of the demodulated signal. The base model we use has two signal outputs and two signal inputs, with the output serving the purpose of the signal generator and the input being the input of the demodulation circuit. the UHFLI also comes with four auxiliary outputs which can be used to stream quantities such as amplitude or phase of the demodulated signal from the UHFLI into another unit, which in our case is the AlazarCard.

When using the UHFLI it is important to be aware of the different sampling speeds of the different units inside it and know what your limitations are. Although the fast digitizer card inside the UHFLI has a maximum sampling speed of 1.8 GS/s, just like our AlazarCard, the demodulation circuit *output* can only operate up to 14 MS/s. As such, the demodulation of the signal is most likely done as fast as the input ADC can sample the rf-signal but after demodulation the signal is then downsampled either by decimation or bandwidth limitation. Downsampling via decimation means chopping up the signal by only saving every N 'th data point and discarding the rest. The bandwidth of the UHFLI is fixed to 600 MHz, so if the sampling speed is reduced to less than 1.2 GS/s the Nyquist sampling criterion is no longer satisfied and we'll have strong aliasing effects in the downsampled signal. Downsampling via bandwidth limitation on the other hand is done by averaging N consecutive points together. Once we start averaging points together instead of discarding them the input signal bandwidth is reduced and as such a high enough

sampling rate to sufficiently satisfy the Nyquist criterion and aliasing effects are suppressed in the downsampled signal.

2.4.3 Sample clock synchronization

Probably the most important kind of synchronization we should be aware of is synchronization of sample clocks in our equipment. Imagine you have two signal generators, e.g. two SRS SG384's, and you want one to output an rf-signal at a frequency f_1 and the other at f_2 . If you do not continuously synchronize the sample clock of the two signal generators, ensuring that the timebase on which the rf-carrier is sampled is the same, then at some point, even if at the beginning they are ensured to be identical, there will be an overall frequency- and/or phase-shift between the two signals even before they leave the signal generator. However it is not only important to synchronize the sample clocks of the signal sources to each other, synchronizing the sample clock of the data acquisition equipment is also important. As such we always connect the 10 MHz clock reference between devices, and at the moment we are using the AWG as our master instrument and having signal generators, UHFLI and digitizer board as slave instruments.

3 Measurements

The chapter is split into three sections, the first being a short introduction to how the double-dot device is characterized in the initial stage of the experiment. The second section focuses on how everything reflectrometry circuit related is characterized, such as finding the resonance frequency and matching resistance as well as setting up charge-sensing. The last section will focus on how this knowledge of the device³, the knowledge of the sensor, and the reflectrometry circuit is put to use.

3.1 Characterization of the device

The purpose of this section is to make interested readers familiar with our procedure for characterizing the devices immediately after the cryostat has reached base temperature. For the actual rf read-out measurements please see [sec. 3.3](#).

Initial characterization The initial characterization of the device consists of a number of things. The very first thing to do is checking whether the wires are actually conducting at base temperature, if they froze out (i.e. became insulating) or perhaps blew up during loading or cooldown. This can easily be done by measuring conductance g through the wire as a function of applied bias voltage V_{SD} via standard lock-in technique. If the device is not conducting a heatload can be applied to determine whether it froze out or if it blew up (or a bondwire came off). This can be done either by turning the MC plate heater on or by connecting the load-lock to the puck. If the device is conductive next thing is to check whether any of the gates are leaking. This can be done in two ways, both involves connecting one or more gate(s) to a Keithley SourceMeter⁴. The Keithley is configured such that the maximal current it can source is in the 10 nA to 100 nA range (also often simply referred to as the compliance). Then the amount of voltage the Keithley can maximally apply is specified (typically a couple hundred microvolts).

³When I say "*the device*" I am always referring to the double-dot device. It is also sometimes referred to as "*the island*".

⁴A Keithley SourceMeter is capable of applying a voltage while sourcing and measuring the current, or by sourcing a specified current letting the Keithley apply the voltage needed.

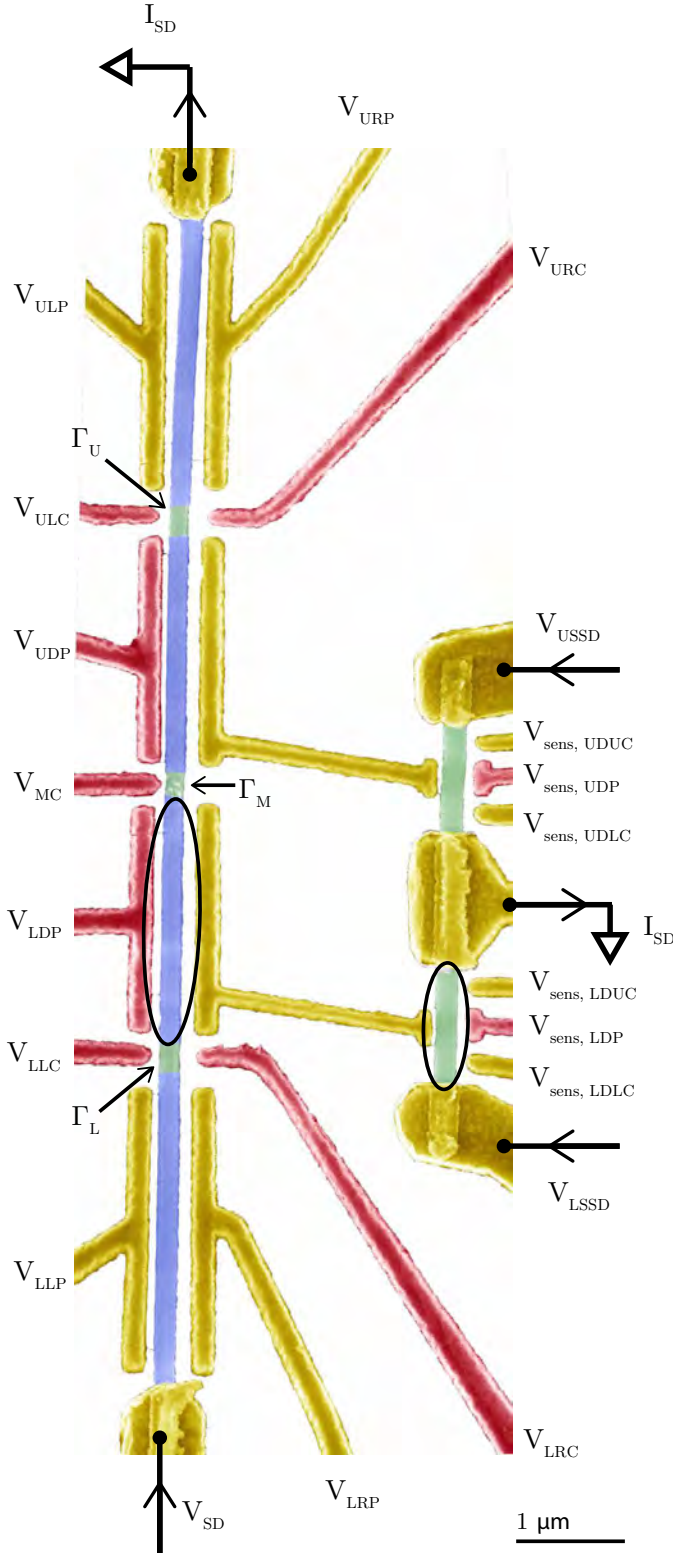


Figure 3.1: Shown is a false-coloured annotated scanning electron micrograph (SEM) of device Q418DR3DDDEV1 used for the experiment. DC Ti/Au gates and contacts (yellow), RF Ti/Au gates (red), epitaxial Al (blue), and InAs (green). Starting from the lower left corner of the SEM image the label V_{LLP} means *lower left plunger*. Going clockwise around the next label V_{LLC} reads *lower left cutter*. Then V_{LDP} is *lower dot plunger*, V_{MC} is *middle cutter*. From here it is the same as before, except the U now refers to *upper* and the R after L/U refers to *right*. Continuing around, the label $V_{(U/L)SSD}$ refers to the *upper/lower sensor source-drain* and e.g. $V_{sens, UDUC}$ refers to the *sensor upper dot, upper cutter*. $\Gamma_{U/M/L}$ indicates the tunneling rates through the upper/middle/lower junction. Black circles indicate where quantum dots are formed. Figure is used courtesy of Dovydas Razmadze.

If the gate is electrically isolated from the environment the resistance to ground will be infinite and the sourced current will be zero and one can turn off the applied voltage and go to a different gate. If a current is flowing the surrounding gates and contacts should be floated one by one until the leak disappears. In the case of a leak one needs to determine which of the gate(s) are more important, only apply a voltage to that gate and keep the other gate(s) floating throughout the experiment.

While the above procedure is fast and puts one in a relatively safe position it is often the case that a substantial voltage applied to the gate is needed before a leak to the environment is observed. As such another way of determining leaks can be used⁵. Instead of going through the gates one-by-one several gates can be hooked up to the same Keithley. The idea is then to monitor the sourced current in the software as the applied voltage is ramped to the desired value (we typically ramp gates to ± 8 V). If the software limit is exceeded the ramp is aborted and the Keithley must manually be ramped to 0 V. One or more gates should be removed from the Keithley and the ramp repeated until no leaks occur and the gates which leak to one-another are identified.

Imagine we have a device similar to **fig. 3.1** and initially all the double-dot device cutters are connected (that is V_{URC} , V_{ULC} , V_{MC} , V_{LLC} , and V_{LRC}) to the Keithley and at 3.8 V a leak is discovered. Then the top-left cutter V_{ULC} could be removed and the ramp repeated. If no leak is discovered then V_{ULC} is leaking to the environment around 3.8 V and should not be operated above that point, but it is still safe to use the gate below it.

E_J vs. E_C Since the devices have both superconducting contacts as well as two superconducting quantum dots, depending on the state of the barriers, that is the ratio of Josephson energy E_J to charging energy E_C , we will see either Josephson physics or Coulomb physics, i.e. supercurrent or Coulomb diamonds. In the regime $E_J \gg E_C$ the number of electrons $n_{1,2}$ in either of the dots is a bad quantum number and instead the phase difference between the superconductors becomes the well-defined quantity for the system. Thus in this regime a supercurrent through

⁵I am personally in favour of this method as it gives you a much better understanding of your experiment and its limitations.

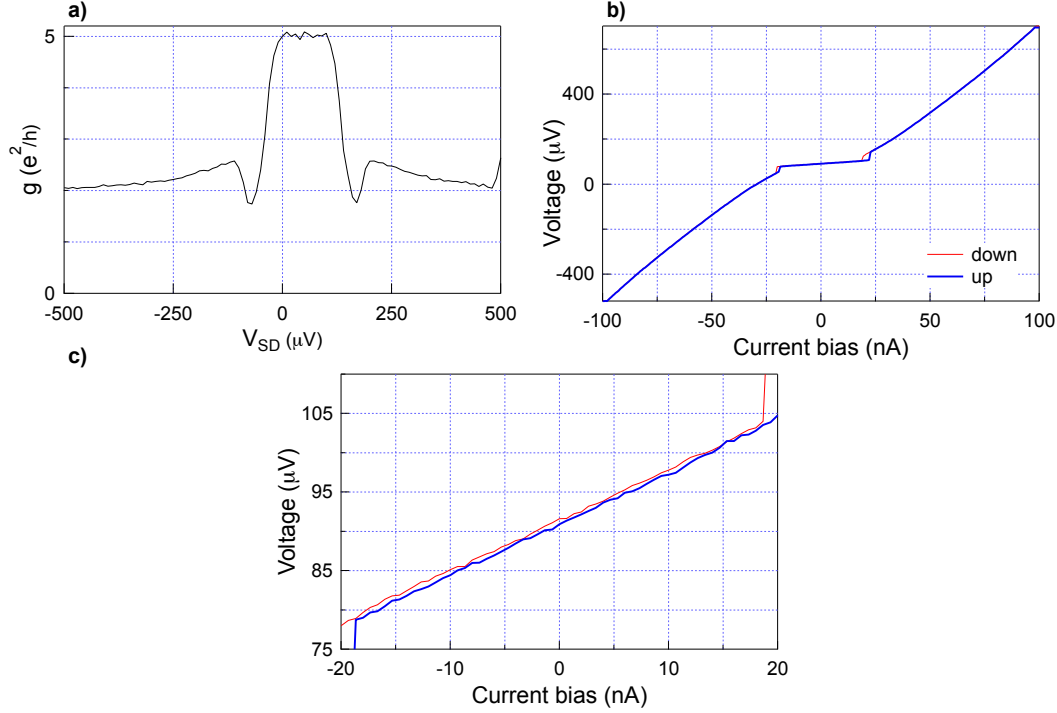


Figure 3.2: Observation of supercurrent in three serially connected Josephson junctions. Panel **a)** shows a voltage-bias measurement of the conductance g through the device. Around zero bias the conductance saturates at $5 e^2/h$ ($\sim 5 k\Omega$). Panel **b)** shows a current-bias measurement of the device sweeping from -100 nA to 100 nA (blue) and from 100 nA to -100 nA (red). Panel **c)** shows a zoom-in of panel **b)**.

the device is observed, see **fig. 3.2**. The current-bias measurement is done by adding a $1 M\Omega$ bias-resistor after the voltage divider. Then, the voltage drop is measured by connecting a BNC cable on the source and the drain, putting them on the two input channels of a SR560 voltage pre-amplifier set to differential mode and connecting the (scaled) output of the pre-amplifier to a DMM. For general fridge-wiring see **appendix. ??**

Performing a current-bias measurement a finite resistance of the about 600Ω is observed inside the superconducting gap. This resistance includes both the junction resistances as well as the lithography which is included in the voltage probes. The reason for this is that the voltage probes are not lithographically connected directly before and after the device, but at the bondpads of the sample board. That means the voltage drop is measured from bondpad to bondpad and

not from the two ends of the device and as such it includes two bondwires and the two lithography lines which connect the bondpads to the sample.

In the other regime $E_J \ll E_C$ the number of electrons $n_{1,2}$ in the two quantum dots are quantized and good quantum numbers and Coulomb blockade physics emerges. For observing quasi-particle poisoning events only a single quantum dot is required and so the double-dot device is tuned into a single dot regime (see **fig. 3.1.**), that is $\Gamma_U \gg \Gamma_M, \Gamma_L$. This regime is reached by applying a large positive voltage to V_{URC} and V_{ULC} and a large negative voltage to V_{MC} , V_{LLC} , and V_{LRC} . Determining if the device is configured to the single-dot regime is most easily checked by doing what is known as a "wall-wall" plot. That is, by scanning the two gates confining the quantum dot while monitoring the conductance through the nanowire at a finite bias either diagonal lines (**fig. 3.5a**) or a typical double-dot honeycomb pattern (not shown) will emerge. One could also scan the bias voltage together with either one of the cutters confining the quantum dot or the plunger gate used to tune the quantum dot density of electrons and look at the Coulomb diamond pattern that emerges (**fig. 3.5b**).

3.2 Characterization of reflectometry

Once the initial characterization of the island wire is over it is time to characterize the reflectometry circuit including the sensor wire. First off it is worth checking whether the sensor dot is responsive to its local gates. If the conductance (or current) through the sensor wire is unchanged even over a large voltage range we do not use it for charge-sensing. Currently a bias voltage is applied to *either* V_{USSD} or V_{LSSD} (with the unbiased contact grounded) and the middle contact is connected to an I/V converter⁶.

Assuming at least one of the two sensor dots is responsive to its local gates characterization of the reflectometry circuit can begin. First off both the parasitic capacitance C_P in the LRC circuit as well as the matching resistance can be determined. Parasitic capacitance can be estimated by measuring the resonance frequency of the two TCs and using (24). Afterwards the matching resistance of

⁶The model we use is a low noise, high stability I/V converter (LNHS IV) from Physics Basel model number SP 983.

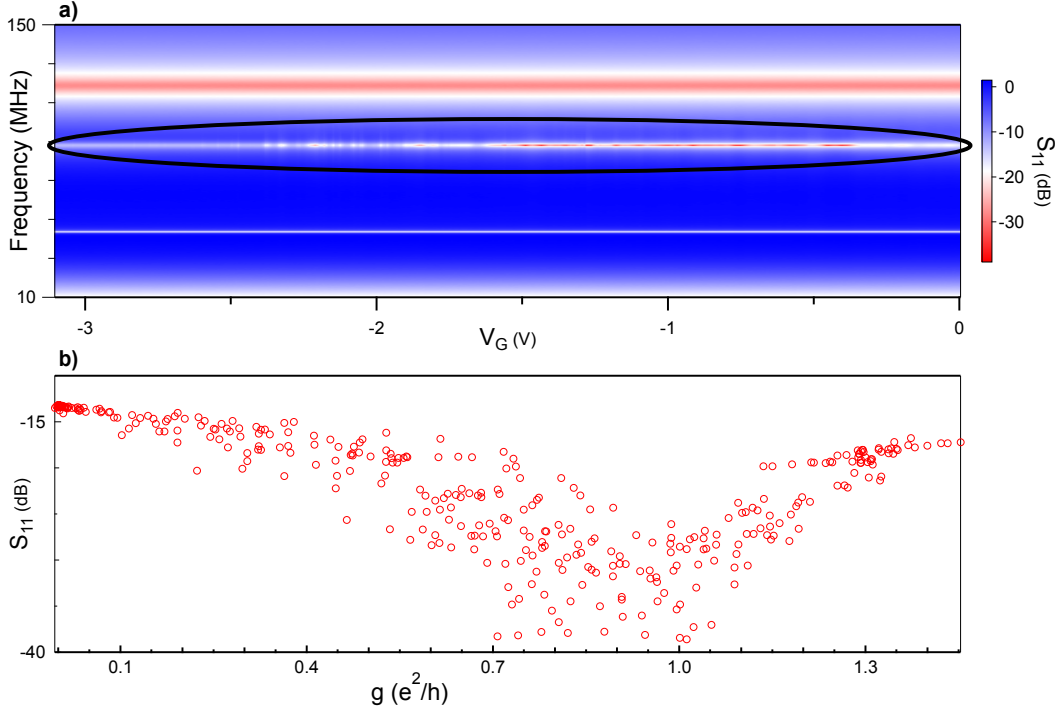


Figure 3.3: Tank circuit resonance changes as a function of applied gate voltage and matching resistance extraction. Panel **a)** shows a landscape of the tank circuit resonances as a function of applied gate voltage to the device gates $V_{\text{sens, LDUC}}$, $V_{\text{sens, LDP}}$, and $V_{\text{sens, LDLC}}$ (see **fig. 3.1** for device layout and gate labels). At each voltage step the reflected signal S_{11} as a function of frequency (VNA) and the conductance g through the nanowire (lock-in, not shown) is recorded. Panel **b)** shows a parametric plot of the reflected signal vs. conductance. The black oval in **a)** indicates the resonance from which S_{11} is extracted. The parametric plot shows a clear correlation between the reflected signal from the tank circuit and the resistance of the nanowire.

the LRC circuit can be determined experimentally by monitoring the reflected signal as well as conductance through the sensor dot as a function of frequency and applied voltage to the local sensor dot gate(s), see **fig. 3.3**.

Setting up charge-sensing The next step is to set up the charge-sensing protocol to be used in **sec. 3.3**. First the sensor wire is tuned into a quantum dot regime with conductance peaks in the range 0.1 to 0.5 e^2/h even though matching occurs between 0.7 and 1 e^2/h . The reason being that as we open up the barriers and increase the conductance Coulomb peaks become lifetime broadened instead

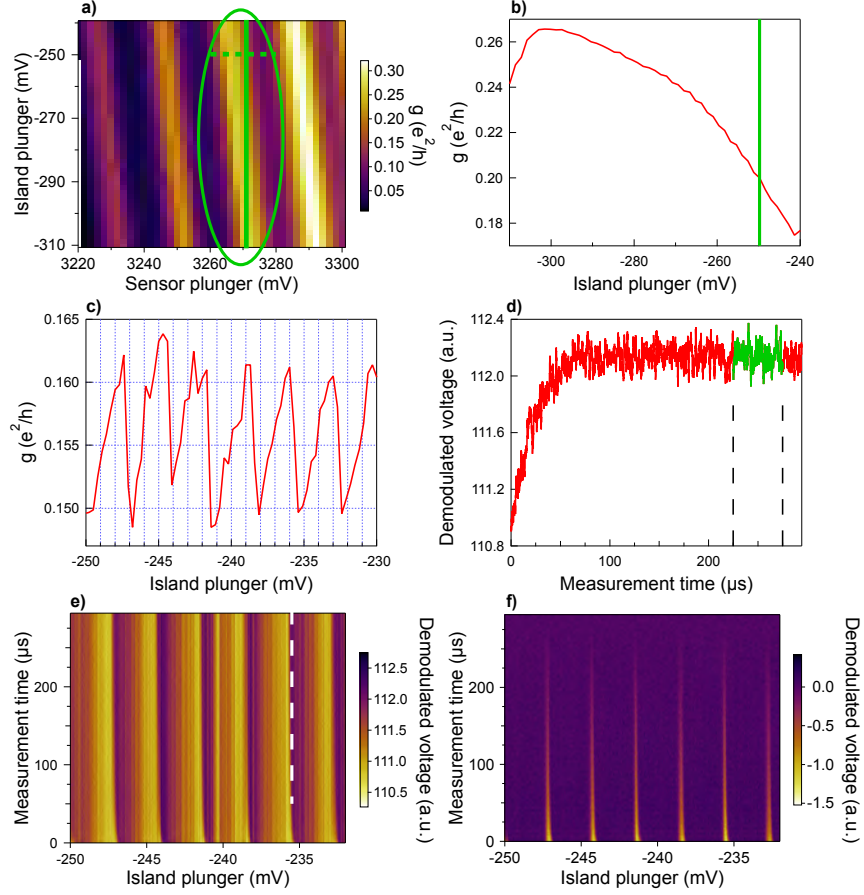


Figure 3.4: Configuration of cross-compensation prior to measuring qpp timescales. Panel **a)** shows a measurement of the conductance g through the sensor wire as a function of the sensor plunger $V_{\text{sens, LDP}}$ and island plunger V_{LDP} . Note that the island plunger in this measurement is *not* cross-compensated. Panel **b)** shows a linecut taken along the solid, vertical green line in **a)**. Green vertical line in **b)** (and dashes horizontal green line in **a)** indicates where cross-compensation is initially configured. Panel **c)** shows conductance g through the sensor wire while sweeping the island plunger using the cross-compensation procedure explained in the main text. Panel **d)** shows linecut from **e)**. Green region marked by dashes lines indicate where the average is calculated for all columns. Dashes white line in **e)** indicates where the linecut is taken. Panel **e)** shows the raw data from an rf-pulse measurement. The reflected signal is monitored as a function of cross-compensated island plunger and measurement time. Near 0 measurement time a small decay to the right (to the left) is observed every time an electron is added to (removed from) the island dot, see e.g. at -235 mV, to the left. Panel **f)** shows processed data of **e)**. Here, the average of the indicated in **d)** is subtracted from the the column. This is done for all columns.

of thermally broadened, i.e. $\hbar(\Gamma_M + \Gamma_B) > k_B T$. Assuming the island wire is tuned into a single-dot regime the next step is to check the cross-coupling of the plunger gate V_{LDP} on the island wire to the states in the sensor wire which is most easily done by sweeping V_{LDP} and $V_{\text{sens, LDLP}}$ while measuring the conductance through the sensor wire, see **fig. 3.4a**. As is evident from **fig. 3.4a**, if cross-compensation of the island plunger using the sensor plunger was *not* done then over a long enough voltage range the charge-sensing signal would disappear as we fall off the conductance peak, see **fig. 3.4b**. For maximal signal-to-noise ratio (SNR) the best place to sit on the conductance peak is where the slope is largest. The green vertical line in **fig. 3.4b** (or dashed horizontal green line in **fig. 3.4a**) indicates the starting point of the cross compensation procedure. Next the vertical slope of the conductance is to be determined which is most easily done by a trial-and-error approach. There are several ways to do the cross-compensation procedure and one such way is shown in **fig. 3.4c**. When a single electron is added to (removed from) the island dot, the effective voltage felt by the resonance level in the sensor dot changes and so the conductance through the sensor changes (see **fig. 3.4c**, the rapid jumps from $0.15 e^2/h$ to $0.16 e^2/h$). Sweeping the island plunger itself also changes the effective voltage felt by the resonance level. In the procedure employed in **fig. 3.4c**, the change in effective voltage from sweeping the island plunger and when adding (removing) an electron from the island wire effectively cancel each other and a saw-tooth signal emerges. Another way to do the cross-compensation would be to completely cancel the effective voltage change induced by changing the voltage on the island plunger, but not compensating the effective voltage change induced by adding or removing an electron. This would lead to QPC-like conductance plateaus. The disadvantage of this is again that after a large enough change in voltage on the island plunger the energy level will no longer be in resonance with the sensor leads and cross-compensation needs to be recalibrated.

3.3 Quasi-particle poisoning events

All the prerequisites required for investigation of the quasi-particle timescale in the system have been outlined and explained so let us now go to the actual pulse experiment. The device is tuned into a single-dot regime (**fig. 3.5**), cross-

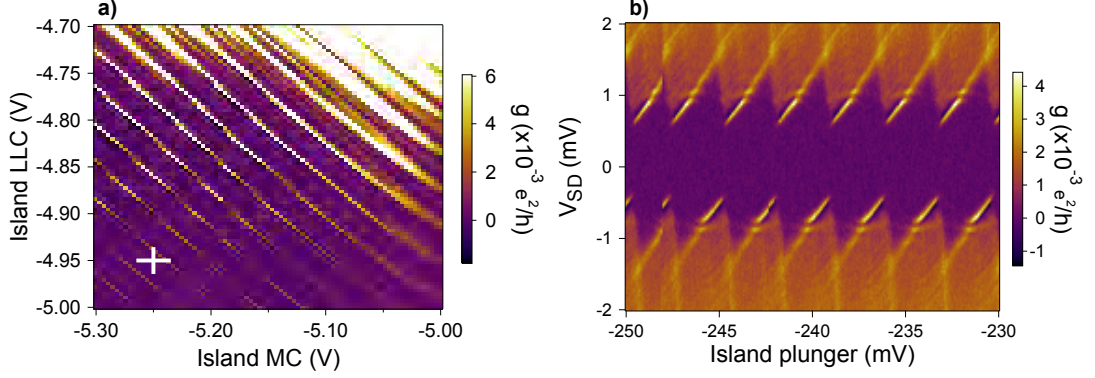


Figure 3.5: Panel **a)** and **b)** shows that the island wire is tuned into a single quantum dot regime. White cross in **a)** indicates where V_{MC} and V_{LLC} are positioned. The gap around zero bias in **b)** is of the order 4Δ as expected for an S-S-S device. High bias conductance indicates that the quantum dot is very weakly coupled to the leads.

compensation is configured (**fig. 3.4c**) and the voltage spacing between saw-tooth steps is similar to the high-bias single electron Coulomb diamonds spacing indicating that even if transport is blocked at zero bias in the island wire, the sensor wire detects the addition of single electrons to the superconducting island. The remainder of the thesis will be focusing on getting a temporal resolution of adding a single electron and investigating the temporal dependence on the coupling to the environment (Γ_M and Γ_B) and temperature.

In the following two pulse sequences will be investigated both shown in **fig. 3.6**. The only difference between the two is whether the dummy pulse segment visible in **fig. 3.6a** is included in the pulse or not. The purpose of the dummy pulse is to ensure that the average amplitude of the whole pulse is zero. As such we avoid potential spurious discharge effects from the bias-tees as well as general heating of the fridge even though the dummy pulse increases the total AC amplitude of the pulse.

Since the bias-tee consists of a resistor and a capacitor it also, unintentionally, behaves as a high-pass filter. This means that if the pulse duration becomes long comparable to the RC time of the bias-tee distortion of the signal reaching the gate will happen. The easiest way to work around this issue is to digitally pre-distort the signal in an inverse manner to the distortion from the bias-tee such that the two will cancel and the pulse reaching the gate is as we intended. This can be

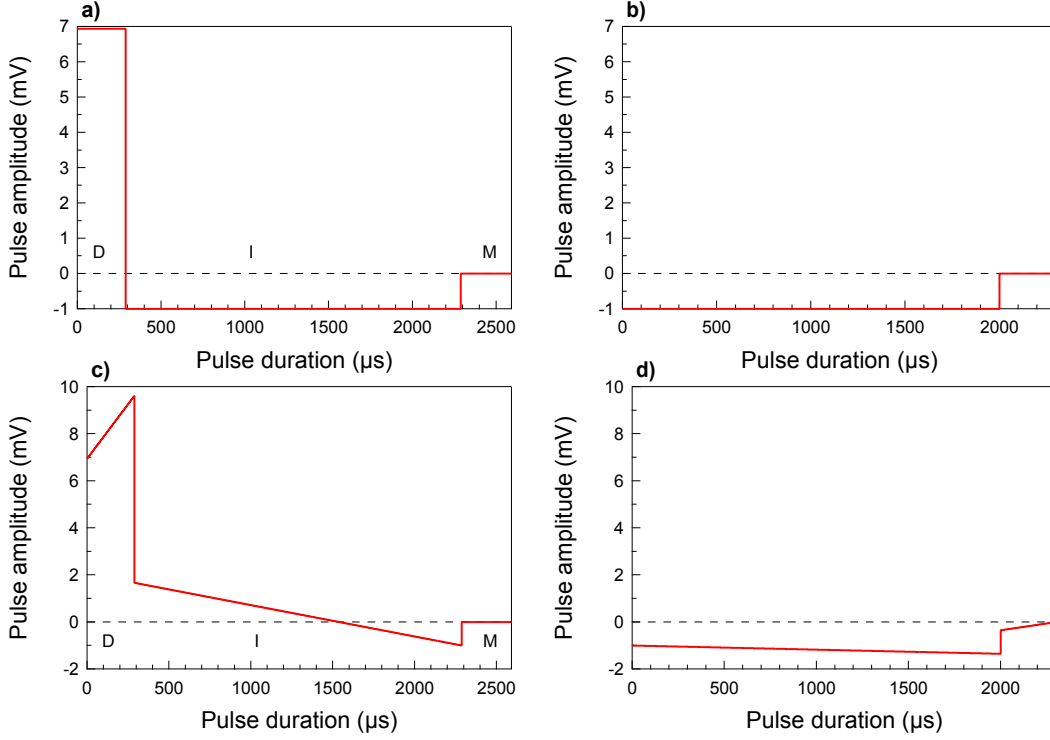


Figure 3.6: Pulse sequence used to investigate quasi-particle poisoning. Panel **a)** and **b)** shows the pulse sequence intended for the experiment with and without the dummy pulse, respectively. Panel **c)** and **d)** shows the actual pulse uploaded to the AWG.

done *in situ* by pulsing up and down one side of a Coulomb peak while monitoring the reflected signal from the TC.

In order to understand the following data let us first focus on the sketch shown in **fig. 3.7**. Here the energy parabolas for a superconducting quantum dot in the $\Delta < E_C$ regime are shown. In the graph four points with three different x -axis positions are indicated, meant as a sketch of where D, I and, M of the pulse sequence takes us. Around the charge degeneracy points a light blue region is filled. This light blue region indicates the 2Δ superconducting gap in the leads. A typical pulse sequence (with D) would for a small amount of time put us in the ground state of where D is. Then, the pulse goes to the initialisation point and eventually the pulse moves to M where the measurement begins. If M is in a region where qpp can occur this will show up in the reflected signal. This region, I think, depends on whether we are adding or removing an electron from the island.

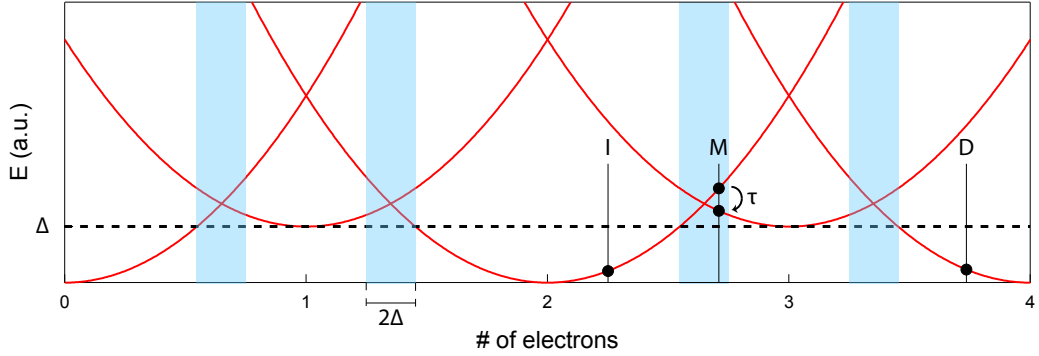


Figure 3.7: Energy diagram for superconducting quantum dot in the regime $\Delta < E_C$. The dummy (D), initialization (I) and measurement (M) positions are sketched. Black circle indicated at I, M, and D is meant as cartoon of an electron with the energy represented by the parabola. At M the QD ground state stays in the upper branch for a time τ until it relaxes into the lower energy state by capturing a QP.

If, as shown in the sketch, we are adding an electron the the relevant region for observing qpp events is at the charge degeneracy point and up to one Δ into the next charge state region. If moved any further the resonance level will be lower than the cooper-pairs in the leads and as such it will always be more energetically favourable to split up a cooper pair (or have cooper-pair exchanges from one lead to the other), and the next resonance level is energetically inaccessible.

Assuming that pulse distortion is calibrated away the investigation of quasi-particle poisoning events can begin.

Coupling dependence Let us start with investigating lead-coupling dependence of the quasi-particle-like decay features that we observe. If both Γ_M and Γ_L are made very small then the sort of reflecomtetry response as the one shown in **fig. 3.4e,f** are observed. That is, a well-behaved system with long qpp timescales.

As the coupling to the leads is increased these qpp features behave differently depending on which lead-coupling you tune. Starting with the lower right cutter (keeping the lower left cutter constant) the data in **fig. 3.8**. As you go from low conductance (weak coupling) to high conductance (strong coupling) the QPP features disappear altogether. However, the decrease does not seem to be monotonically decreasing in a systematic way (compare e.g. **c**) and **e**) in **fig. 3.8**).

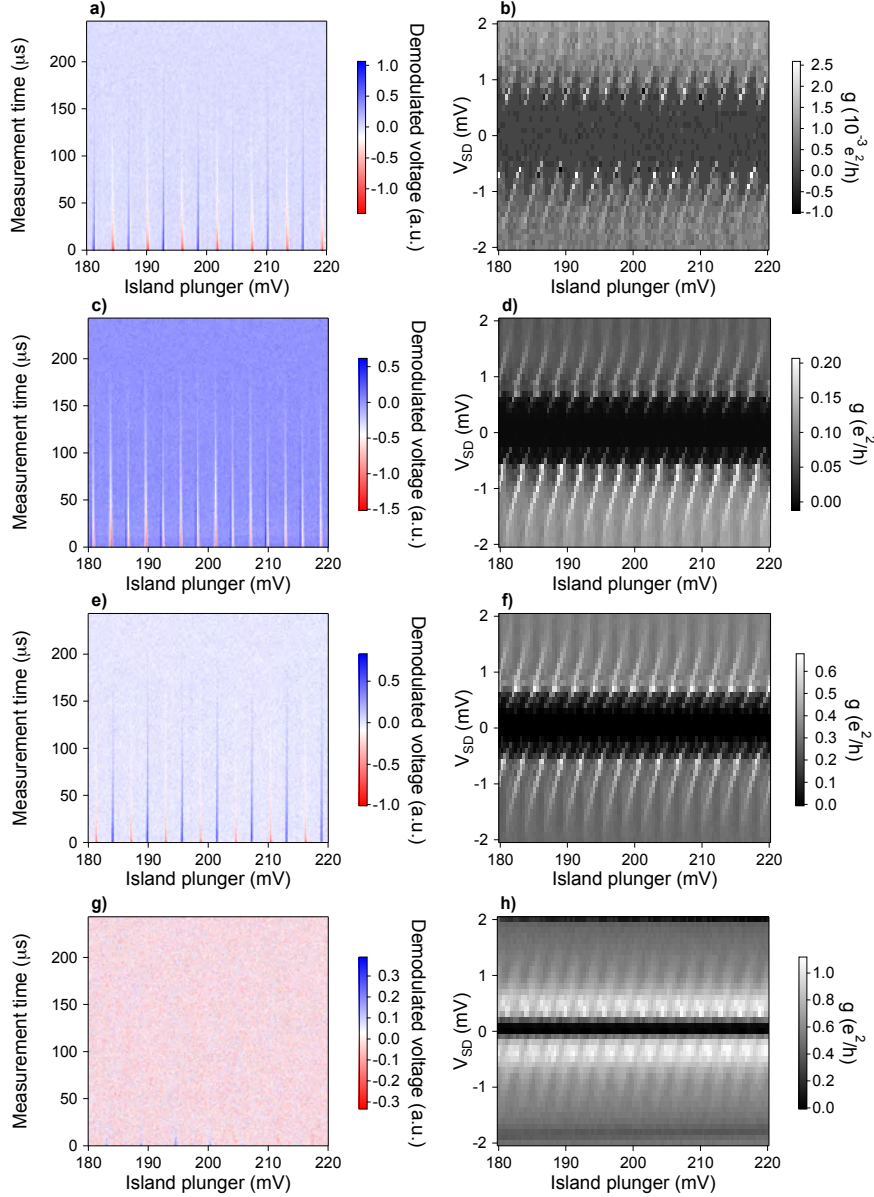


Figure 3.8: Panels a), c), e), and g) show how the qpp timescales changes as the coupling to the lower lead right lead is increased. The dependence is not yet fully understood (compare e.g. c) and e). Panels a), c), e), and g) show the conductance through the island for that gate configuration.

Why it is so is not yet well understood. Furthermore from **fig. 3.8** there is a certain even-odd (or parity) dependence of the behaviour of the qpp events. One interpretation could be that while the system is being initialized we were not

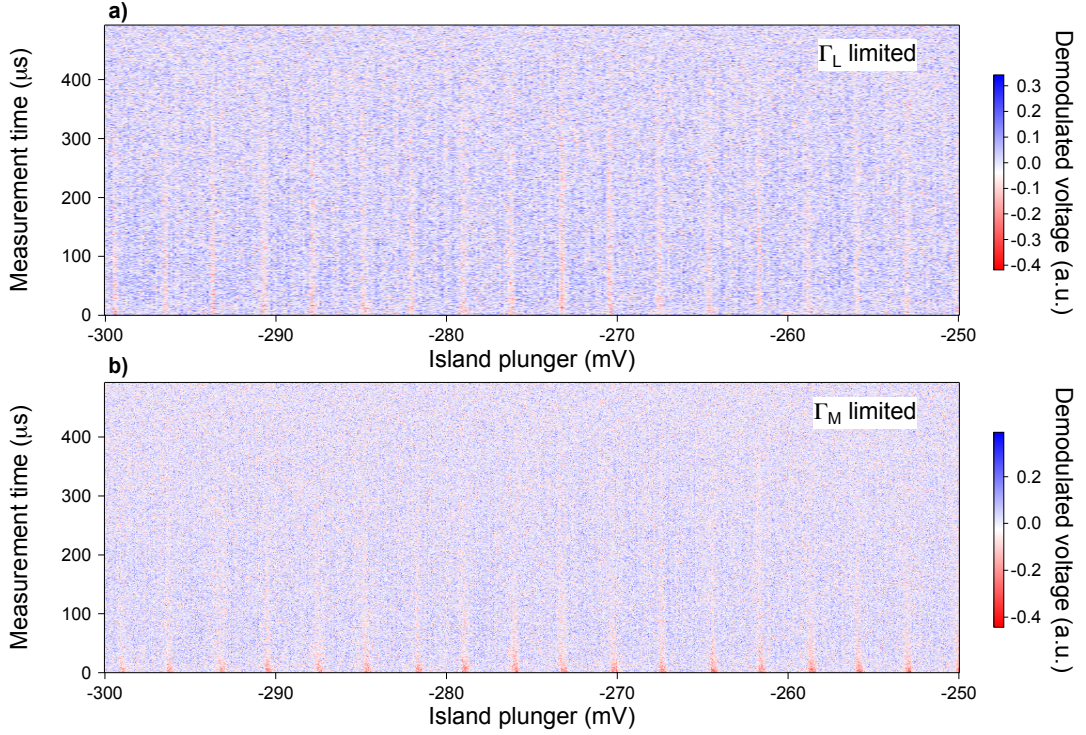


Figure 3.9: Comparison of the qpp timescales for near-identical conductance tunings of the island wire but with either Γ_L (a)) or Γ_M (b)) the limiting coupling factor in the system.

initialising long enough to ensure that the system relaxed into the ground-state before the measurement took place. We have investigated this in a different tuning and were able to show that the parity effect disappeared as the initialization time was increased beyond 600 μs , see **fig. 3.10**.

Next we configure the device in the same overall conductance state but pick either Γ_L or Γ_M as the strongly coupled lead. Doing so we get two different timescales, one being $\sim 50 \mu\text{s}$ ($\Gamma_M > \Gamma_L$) the other being $\sim 0 \mu\text{s}$ ($\Gamma_M < \Gamma_L$), see **fig. 3.9**.

Temperature dependence Besides lead-coupling dependence a mechanism which should also show controllable effect on the qpp timescales is temperature. As we increase the temperature of the system, the quasi-particles get more kinetic energy and resonance states become thermally broadened. All in all as the temperature in-

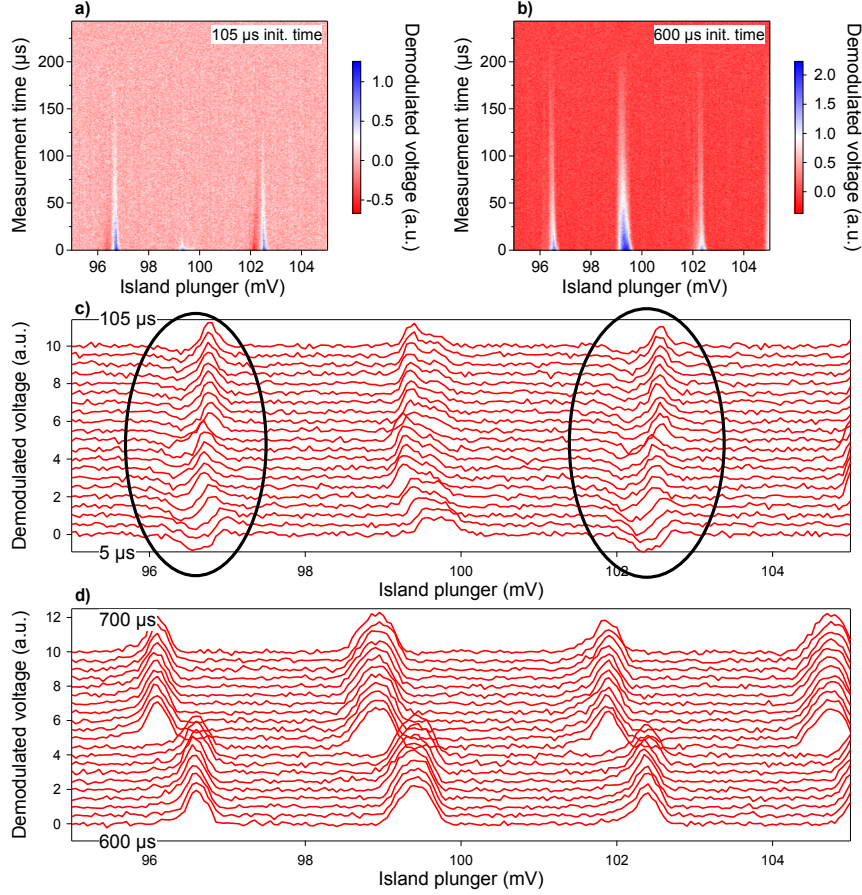


Figure 3.10: Investigation of initialisation-time dependence for parity-dependent quasi-particle poisoning. Panel **a)** and **b)** show two typical 2D images taken while stepping the initialisation time in steps of 5 μs . Panel **c)** and **d)** show linecuts extracted from these 2D images at 0 μs measurement time. Each linecut is offset for clarity. It seems that the initialization time is increased from 10s of μs to several hundred μs the parity-dependence disappears.

creases we would expect to see a decrease in the quasi-particle poisoning timescale. In **fig. ??** and **fig. 3.12** we investigate the temperature dependence going from base temperature (16 mK) all the way to 800 mK.

Sanity checks Here I will mention two sanity checks we have performed in the same tuning as the temperature dependence is measured. This is to check the robustness of our measurements and ensuring no spurious, unexpected effects are being introduced by (1) including or excluding the dummy pulse segment and (2)

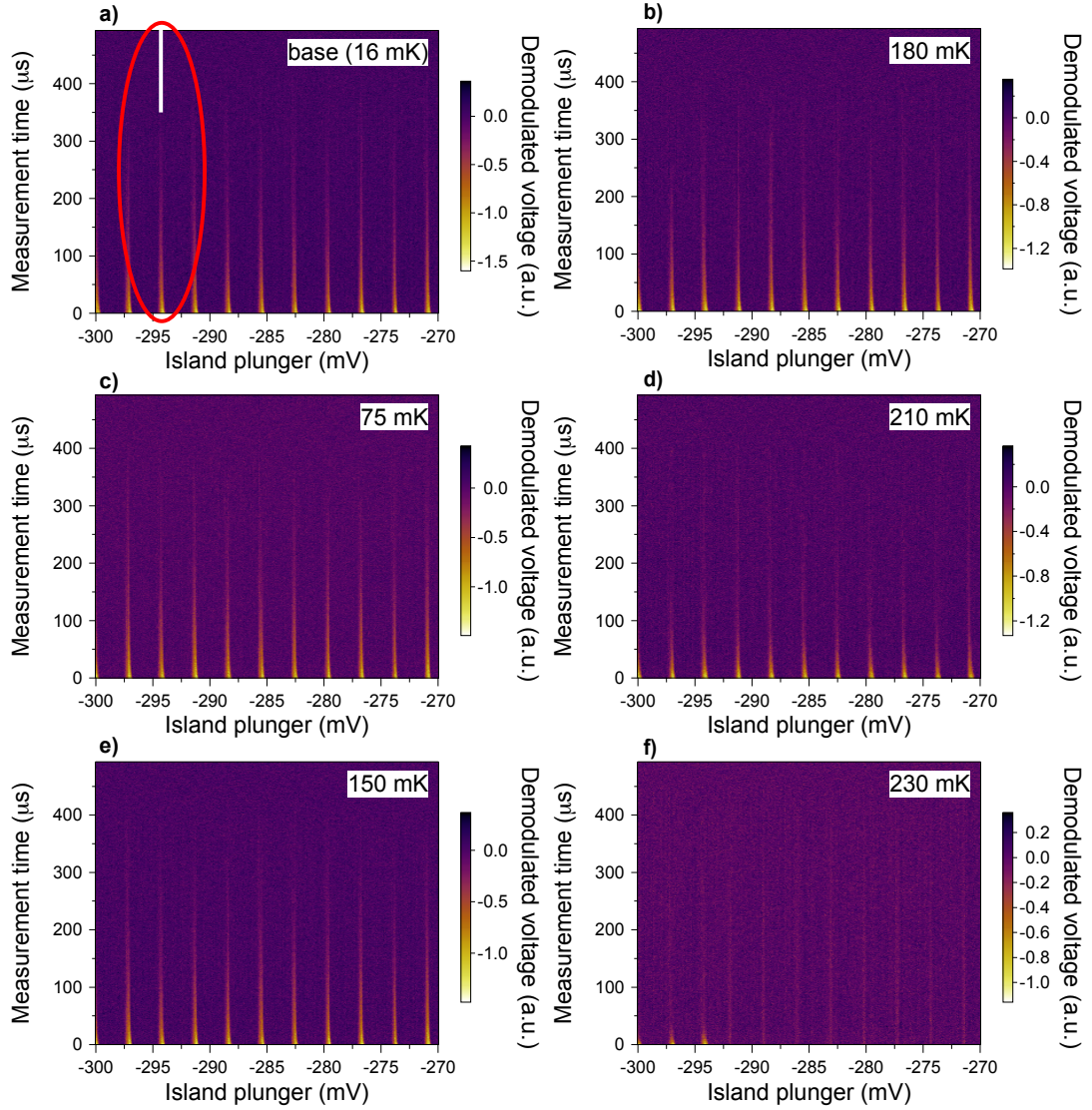


Figure 3.11: Temperature dependence of the quasi-particle poisoning time. All three panels show the post-processed data of the reflected signal as a function of island plunger gate with rf-pulse on top. Panel a) is taken at base temperature (16 mK on the MC plate). Red circle indicates which peak the qpp times are extracted from for all datasets. White bar gives rough indication of where in the peak a vertical linecut is taken. Panel c) is taken at 75 mK, panel e) at 150 mK, panel b) at 180 mK, panel d) at 210 mK, and panel f) at 230 mK.

too short an initialisation time. If halving the initialisation time would systematically introduce other effects than just what we attribute to poisoning events 2

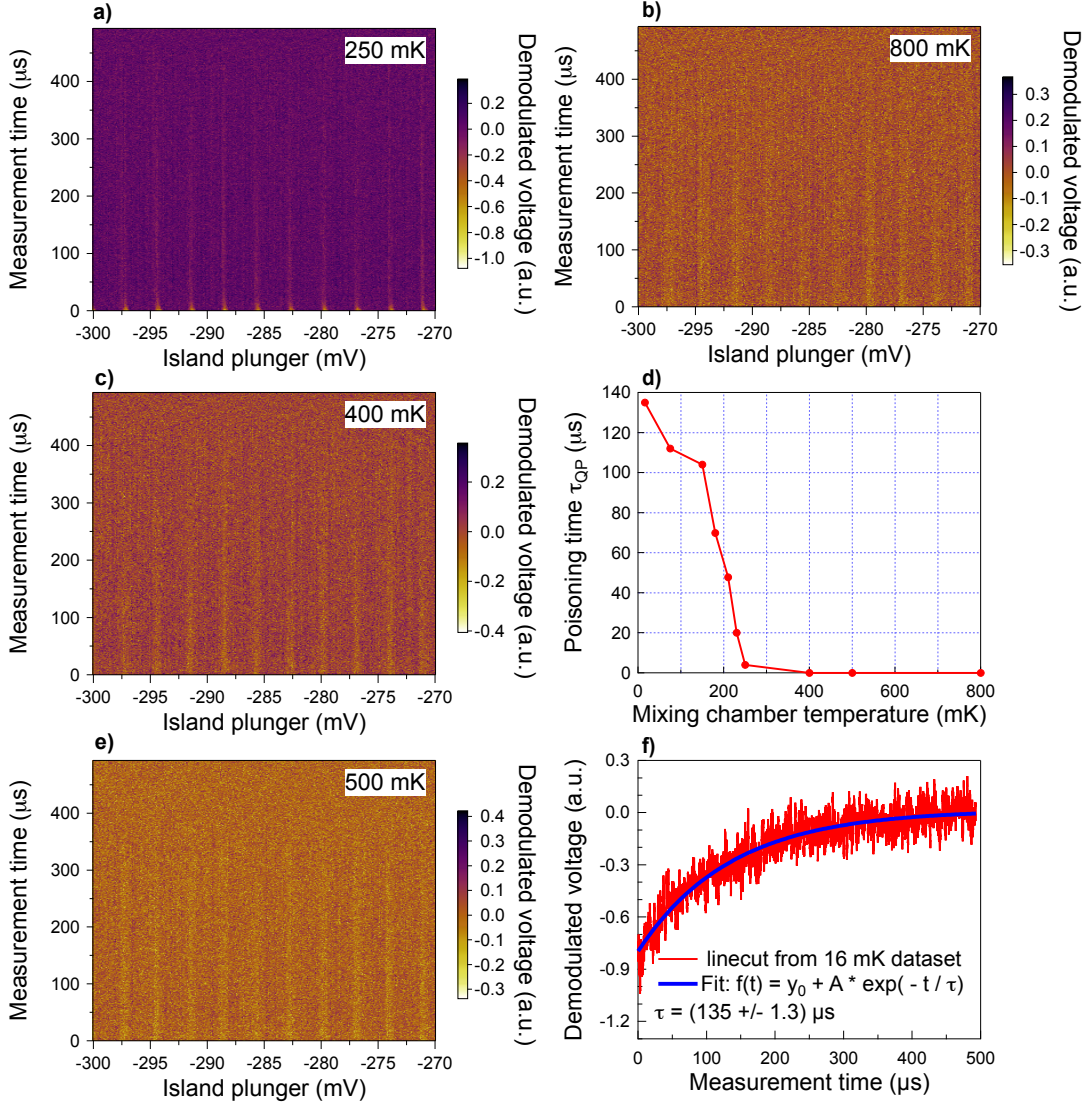


Figure 3.12: Temperature dependence of the quasi-particle poisoning time. Panel a) to c) and f) show the post-processed data of the reflected signal as a function of island plunger gate with rf-pulse on top. Panel a) is taken at 250 mK, b) at 400 mK, c) at 500 mK, and f) at 800 mK. Panel d) shows the quasi-particle time extracted from the peak indicated in fig. ??a. Error bars not shown due to being hidden in the markers. Panel f) shows a linecut taken from fig. ??a indicated by vertical white line.

ms would not have been a good choice of initialisation time for the experiment. Furthermore, it is somewhat surprising that inverting the pulse sequence and thus turning the experiment from a poisoning experiment to an *un*-poisoning experi-

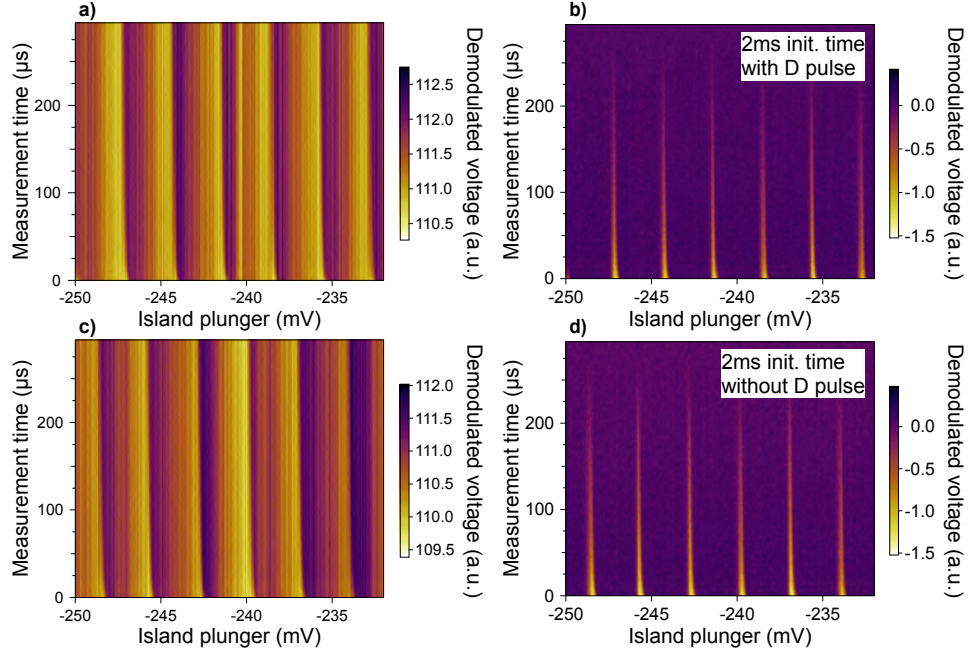


Figure 3.13: Investigating of whether including the dummy pulse segment introduces unwanted effects or not. Panel **a)** and **b)** shows the raw and post-processed data, respectively, for a pulse sequence which identical to the one seen in **fig. 3.6c**. Initialisation time is 2 ms. Panel **c)** and **d)** shows the raw and post-processed data, respectively, for the same pulse sequence but omitting the dummy pulse segment, identical to the sequence shown in **fig. 3.6d**. No change in the data is observed.

ment does not seem to affect the timescale at all. The only observable change in the dataset is the decay observed in the region 0 to 20 μs measurement time which, for the poisoning experiment bends to the right of the peak, but for the unpoisoning experiment bends to the left. This signature is what makes me believe the only place we should expect to see qp events, when looking that the energy parabolas of the quantum dot, is within one Δ to the right of the charge degeneracy point.

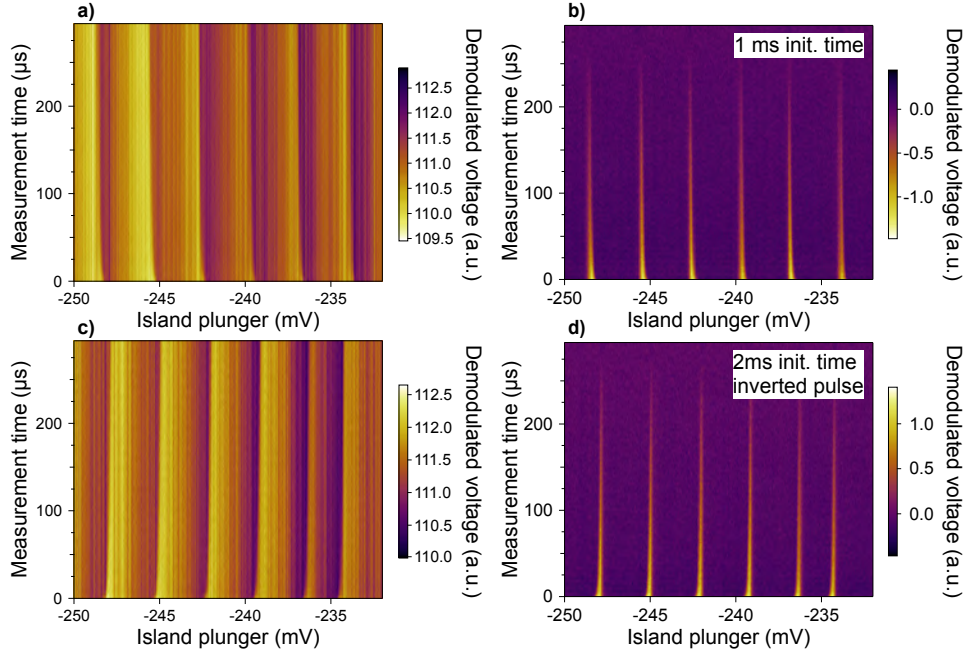


Figure 3.14: Investigation of whether halving the initialisation time or inverting the pulse signal introduces unexplainable effects. Panel **a)** and **b)** shows the raw and post-processed data, respectively, of the qpp time but cutting initialisation time in half compared to the temperature dependence. Panel **c)** and **d)** shows raw and post-processed data, respectively of the qpp time if the pulse is inverted. Except for the flip of the decay in panel **d)** compared to **b)** (look near 0 measurement time) no change is observed.

4 Conclusion

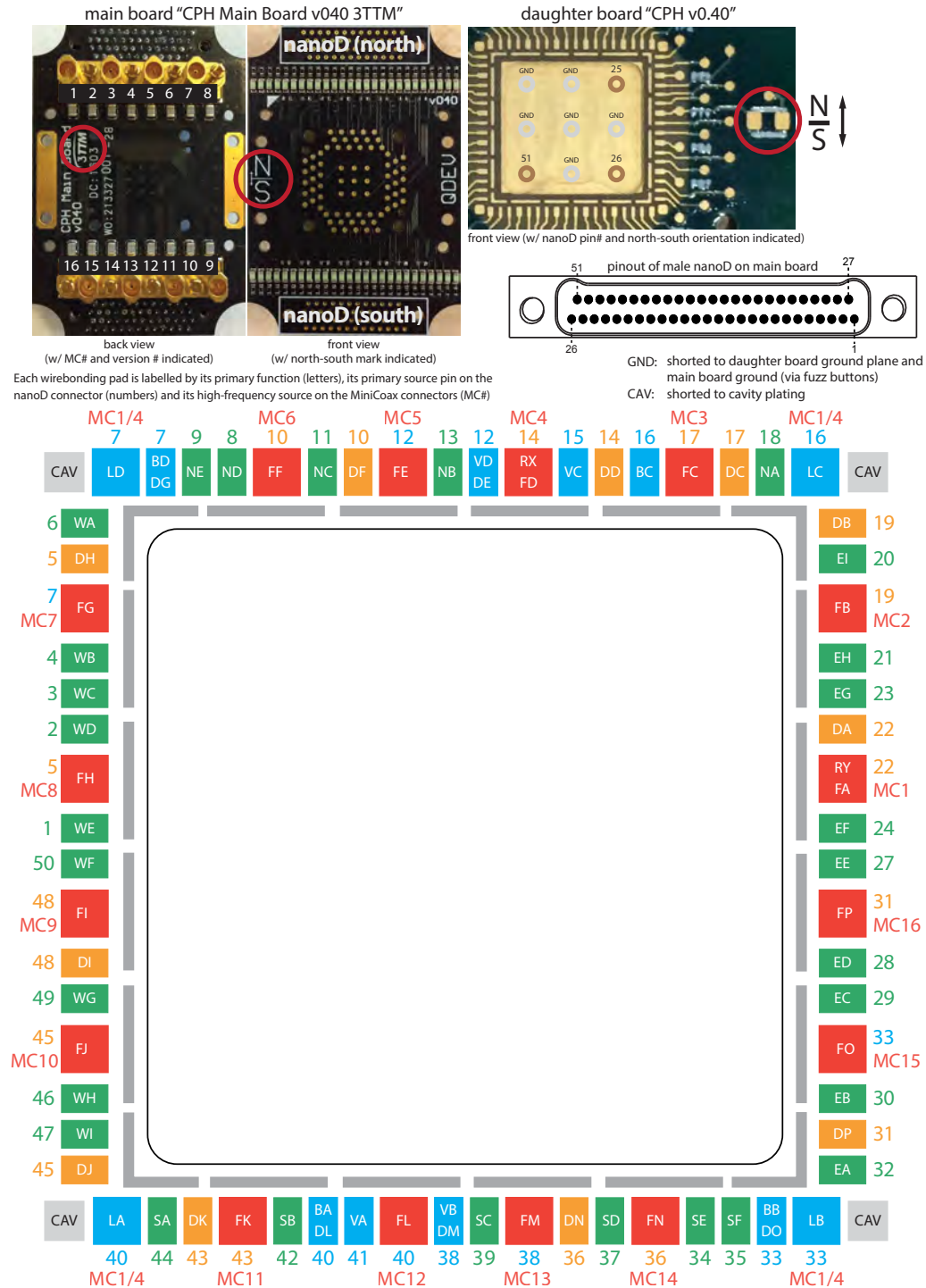
In this thesis the first set of the next-generation nanowire-based superconductor-semiconductor nanostructures is investigated. The data is acquired using a new, previously untested for use with rf signals, modular sample system in the new laboratory at the Center for Quantum Devices. First I show that using a dogbone coupler between the quantum dot and sensor dot we are able to detect adding (subtracting) single electrons to (from) the quantum dot.

Next I show that our S-I-S-I-S-I-S devices can be tuned from a Josephson regime deep into a single quantum dot regime. With the device in deep Coulomb blockade, the dependence of the quasi-particle poisoning time on temperature and coupling to the leads is investigated. Starting at base temperature (16 mK) and a quasi-particle poisoning time of 135 μ s the quasi-particle poisoning time decreases monotonically until it happens instantaneously at 400 mK or above.

It is further shown that the quasi-particle poisoning time is Γ_L limited and poisoning from the top lead (strongly coupled to the upper quantum dot) is not the limiting timescale in the system.

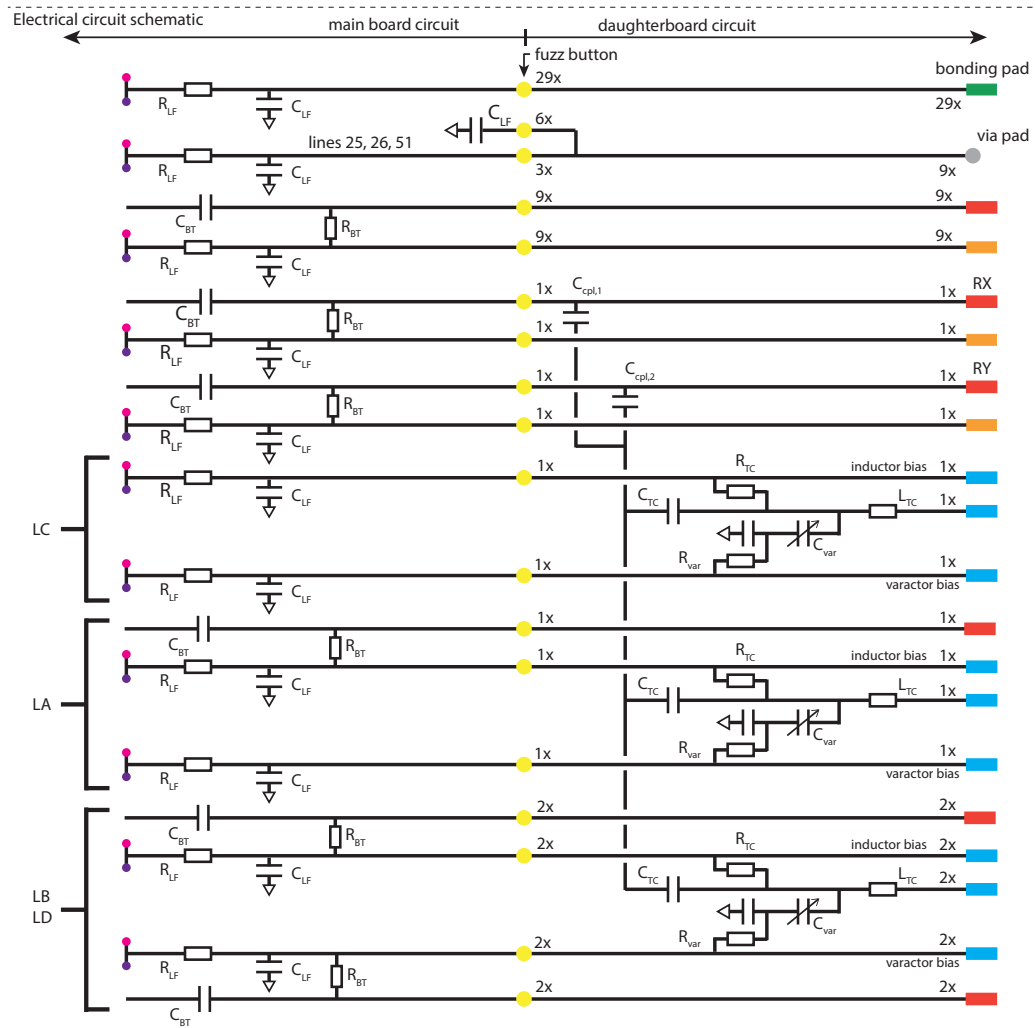
Sanity checks are made to ensure the robustness of the observed features. Taking a dataset in a given voltage range both with and without a dummy pulse as well as doubling and halving the initialization time does not change the observed features. Inverting the pulse (still without the dummy pulse) inverts the observed features as we expect.

A Pinout of Copenhagen sample board



Details of "CPH v0.40" daughterboard pinout

code:	function:
grey	= floating helper pad
F_	= fast pad
D_	= DC bias of fast pad
V_	= varactor DC bias (monitor)
L_	= inductor sensing pad
B_	= bias of inductor (monitor)
RX, RY	= use one of them to read reflectometry circuit (via SMD capacitor), use the other as fast pad
N_, W_, S_, E_	= slow pads (North, West, South, East)



*note that the daughterboard has four tank circuits in parallel, with all four having MC1 or MC4 as their input RF source depending on whether C_{cpl1} or C_{cpl2} is soldered. Individual tank circuits can be removed or installed by either adding or removing the tank circuit capacitor C_{TC}

- nanoD (north)
- nanoD (south)

B Fridge wiring

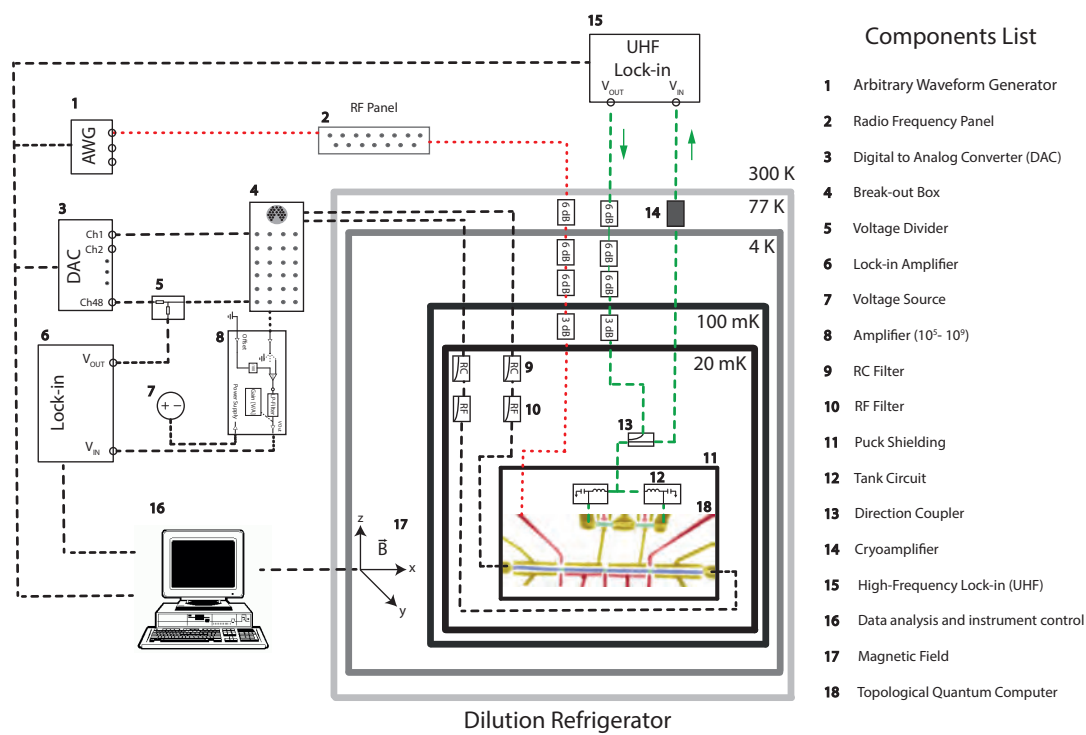


Figure B.1: Schematic showing how the setup is configured from data acquisition PC all the way down to the sample. Schematic courtesy of Dovydas Razmadze.

References

- [1] S. M. Albrecht et al. “Exponential protection of zero modes in Majorana islands”. In: *Nature* 531.7593 (Mar. 2016), pp. 206–209.
- [2] D. Aasen et al. “Milestones toward Majorana-based quantum computing”. In: *ArXiv e-prints* (Nov. 2015). arXiv: [1511.05153 \[cond-mat.mes-hall\]](#).
- [3] J Majer et al. “Coupling superconducting qubits via a cavity bus”. In: *Nature* 449.7161 (Sept. 2007), pp. 443–447.
- [4] I Chiorescu et al. “Coherent dynamics of a flux qubit coupled to a harmonic oscillator”. In: *Nature* 431.7005 (Sept. 2004), pp. 159–162.
- [5] S. I. Kiselev et al. “Microwave oscillations of a nanomagnet driven by a spin-polarized current”. In: *Nature* 425 (Sept. 2003), pp. 380–383.
- [6] J. E. Mooij et al. “Josephson Persistent-Current Qubit”. In: *Science* 285.5430 (Aug. 1999), pp. 1036–1039.
- [7] L DiCarlo et al. “Demonstration of two-qubit algorithms with a superconducting quantum processor”. In: *Nature* 460.7252 (Sept. 2009), pp. 240–244.
- [8] F. H. L. Koppens et al. “Driven coherent oscillations of a single electron spin in a quantum dot”. In: *Nature* 442.7104 (Aug. 2006), pp. 766–771.
- [9] J. H. Kastner et al. “An X-ray outburst from the rapidly accreting young star that illuminates McNeil’s nebula”. In: *Nature* 430.6998 (July 2004), pp. 429–431.
- [10] R Hanson et al. “Spins in few-electron quantum dots”. In: *Reviews of Modern Physics* 79.4 (Oct. 2007), pp. 1217–1265.
- [11] J. R. Petta et al. “Coherent Manipulation of Coupled Electron Spins in Semiconductor Quantum Dots”. In: *Science* 309.5744 (Sept. 2005), pp. 2180–2184.
- [12] G. K. Brennen et al. “Quantum Logic Gates in Optical Lattices”. In: *Physical Review Letters* 82.5 (Feb. 1999), pp. 1060–1063.
- [13] E Knill, R Laflamme, and G. J. Milburn. “A scheme for efficient quantum computation with linear optics”. In: *Nature* 409 (Jan. 2001), pp. 46–52.

-
- [14] R. J. Levis. “Selective Bond Dissociation and Rearrangement with Optimally Tailored, Strong-Field Laser Pulses”. In: *Science* 292.5517 (Mar. 2001), pp. 709–713.
 - [15] E Giraud et al. “Legumes Symbioses: Absence of Nod Genes in Photosynthetic Bradyrhizobia”. In: *Science* 316.5829 (June 2007), pp. 1307–1312.
 - [16] G. Balasubramanian et al. “Ultralong spin coherence time in isotopically engineered diamond”. In: *Nature Materials* 8.5 (Apr. 2009), pp. 383–387.
 - [17] C Monroe et al. “Demonstration of a Fundamental Quantum Logic Gate”. In: *Physical Review Letters* 75 (Dec. 1995), pp. 4714–4717.
 - [18] D Leibfried et al. “Quantum dynamics of single trapped ions”. In: *Reviews of Modern Physics* 75 (Mar. 2003), pp. 281–324.
 - [19] F Jiao et al. “Selective conversion of syngas to light olefins”. In: *Science* 351.6277 (Mar. 2016), pp. 1065–1068.
 - [20] D Kielpinski, C Monroe, and D. J. Wineland. “Architecture for a large-scale ion-trap quantum computer”. In: *Nature* 417 (June 2002), pp. 709–711.
 - [21] C Monroe et al. “A ”Schödinger Cat” Superposition State of an Atom”. In: *Science* 272 (May 1996), pp. 1131–1136.
 - [22] F. Schmidt-Kaler et al. “Realization of the Cirac–Zoller controlled-NOT quantum gate”. In: *Nature* 422 (Mar. 2003), pp. 408–411.
 - [23] D. G. Cory et al. “NMR Based Quantum Information Processing: Achievements and Prospects”. In: *Fortschritte der Physik* 48 (2000), pp. 875–907. eprint: [quant-ph/0004104](#).
 - [24] I. Chuang et al. “Experimental realization of a quantum algorithm”. In: *Nature* 393 (May 1998), pp. 143–146.
 - [25] L. M. K. Vandersypen et al. “Experimental realization of Shor’s quantum factoring algorithm using nuclear magnetic resonance”. In: *Nature* 414 (Dec. 2001), pp. 883–887.
 - [26] M. Steffen et al. “Experimental Implementation of an Adiabatic Quantum Optimization Algorithm”. In: *Physical Review Letters* 90 (Feb. 2003), p. 067903.

REFERENCES

- [27] A. F.F.T.F. H. David G Cory. “Ensemble Quantum Computing by NMR Spectroscopy”. In: *Proceedings of the National Academy of Sciences of the United States of America* 94.5 (1997), pp. 1634–1639.
- [28] I. Bloch. “Ultracold quantum gases in optical lattices”. In: *Nature Physics* 1 (Oct. 2005), pp. 23–30.
- [29] T. Farrow, R. A. Taylor, and V. Vedral. “Towards witnessing quantum effects in complex molecules”. In: *Faraday Discuss.* 184 (0 2015), pp. 183–191.
- [30] D. P. Divincenzo. “The Physical Implementation of Quantum Computation”. In: *Fortschritte der Physik* 48 (2000), pp. 771–783. eprint: [quant-ph/0002077](#).
- [31] E. Majorana. In: *Nuovo Cimento* 5 (1937), 171–184.
- [32] A. Y. Kitaev. “Fault-tolerant quantum computation by anyons”. In: *Annals of Physics* 303 (Jan. 2003), pp. 2–30. eprint: [quant-ph/9707021](#).
- [33] C. Nayak et al. “Non-Abelian anyons and topological quantum computation”. In: *Rev. Mod. Phys.* 80 (3 2008), pp. 1083–1159.
- [34] V. Mourik et al. “Signatures of Majorana Fermions in Hybrid Superconductor-Semiconductor Nanowire Devices”. In: *Science* 336.6084 (2012), pp. 1003–1007. ISSN: 0036-8075.
- [35] L. P. Rokhinson, X. Liu, and J. K. Furdyna. “The fractional a.c. Josephson effect in a semiconductor–superconductor nanowire as a signature of Majorana particles”. In: *Nature Physics* 8.11 (Sept. 2012), pp. 795–799.
- [36] M. T. Deng et al. “Anomalous Zero-Bias Conductance Peak in a Nb–InSb Nanowire–Nb Hybrid Device”. In: *Nano Letters* 12.12 (2012), pp. 6414–6419.
- [37] H. K. Onnes. “Further experiments with liquid helium. C. On the change of electric resistance of pure metals at very low temperatures etc. IV. The resistance of pure mercury at helium temperatures”. In: *Through Measurement to Knowledge: The Selected Papers of Heike Kamerlingh Onnes 1853–1926*. Ed. by K. Gavroglu and Y. Goudaroulis. Dordrecht: Springer Netherlands, 1991, pp. 261–263. ISBN: 978-94-009-2079-8.

- [38] B. D. Josephson. “Possible new effects in superconductive tunnelling”. In: *Physics Letters* 1 (1962), pp. 251–253.
- [39] A. V. Feshchenko et al. “Tunnel-Junction Thermometry Down to Millikelvin Temperatures”. In: *Phys. Rev. Applied* 4 (3 2015), p. 034001. <http://link.aps.org/doi/10.1103/PhysRevApplied.4.034001>.
- [40] *Precision thin film product overview*. Accessed July 7th 2016. page 4. Vishay Intertechnology, Inc. <http://www.vishay.com/docs/49562/49562.pdf>.
- [41] S. Chaudhuri et al. “Fabrication of superconducting tantalum nitride thin films using infra-red pulsed laser deposition”. In: *ArXiv e-prints* (Feb. 2013). arXiv: [1302.4579](https://arxiv.org/abs/1302.4579) [[cond-mat.supr-con](#)].
- [42] M. Kufahl. “Experimental Methods for Implementing Electron Spin Qubits in Double Quantum Dots”. MA thesis. Copenhagen: Niels Bohr Institute, University of Copenhagen, 2014.
- [43] T. Larsen. “Dispersive Readout in Mesoscopic Structures”. MA thesis. Copenhagen: Niels Bohr Institute, University of Copenhagen, 2013.